In Search of Transcriptomic Correlates of Neuronal Firing-Rate Adaptation across Subtypes, Regions and Species: A Patch-seq Analysis

John Hongyu Meng[1†], Yijie Kang[1,9†], Alan Lai[1], Michael Feyerabend[3,4], Wataru Inoue[2,3], Julio Martinez-Trujillo[2,3,4], Bernardo Rudy[5,6,7], Xiao-Jing Wang[1*]

[1]Center for Neural Science, New York University, New York, 10003, NY, United States.
[2]Department of Physiology and Pharmacology, Western University, London, ON N6A 3K7, Ontario, Canada.
[3]Robarts Research Institute, Western University, London, ON N6A 3K7, Ontario, Canada.
[4]Schulich School of Medicine and Dentistry, Western University, London, ON N6A 3K7, Ontario, Canada.
[5]Neuroscience Institute, New York University Grossman School of Medicine, New York, 10016, NY, United States.
[6]Department of Neuroscience and Physiology, New York University Grossman School of Medicine, New York, 10016, NY, United States.
[7]Department of Anesthesiology, Perioperative Care and Pain Medicine, New York University Grossman School of Medicine, New York, 10016, NY, United States.
[8]Department of Anesthesiology, Perioperative Care and Pain Medicine, New York University Grossman School of Medicine, New York, 10016, NY, United States.
[9]Current address: Graduate School, Stony Brook University, Stony Brook, 11794, NY, United States.

*Corresponding author(s). E-mail(s): xjwang@nyu.edu
†These authors contributed equally to this work.

Abstract: Can the transcriptomic profile of a neuron predict its physiological properties? Using a Patch-seq dataset of the primary visual cortex, we addressed this question by focusing on spike rate adaptation (SRA), a well-known phenomenon that depends on small conductance calcium (Ca)-dependent potassium (SK) channels. We first show that in parvalbumin-expressing (PV) and somatostatin-expressing (SST) interneurons (INs), expression levels of genes encoding the ion channels underlying action potential generation are correlated with the half-width (HW) of spikes. Surprisingly, the SK encoding gene is not correlated with the degree of SRA (dAdap). Instead, genes that encode proteins upstream from the SK current are correlated with dAdap, a finding validated by a different dataset from the mouse's primary motor cortex that includes pyramidal cells and interneurons, as well as physiological datasets from multiple regions of macaque monkeys. Finally, we construct a minimal model to reproduce observed heterogeneity across cells, with testable predictions.

1 Introduction

With the advances in the brain connectome and the simultaneous recording from multiple brain areas in behaving animals, studies of the large-scale multiregional brain has come to the fore [54]. To understand the brain-wide dynamics, it is necessary to consider differences in the electrophysiological features of single neurons in disparate areas. However, single-cell physiological studies such as patch-clamp measurements are costly; at the present time there is a dearth of systematical comparison of single cell physiological characteristics across many brain regions. On the other hand, single-cell transcriptomic analysis bas become common and offers a novel approach to quantification of the brain [27, 12, 48]. So far, this tool has been mostly deployed for cell type classification. Can transcriptomic profile predicts physiological properties of single cells? The answer is not obvious, as there are multiple intermediate steps from mRNAs to proteins to physiological functions of receptors and ion channels. In this work, we tackled this challenging question by focusing on single-neuron spike rate adaptation, a salient characteristic of firing patterns in distinct subtypes of neurons.

The development of Patch-seq marks a significant advancement in correlating transcriptomic data with single-cell electrophysiological features [33]. Unlike quantitative real-time PCR (RT-PCR), which is limited to studying specific genes with high accuracy [45], and single-cell RNA sequencing (scRNA-seq), which provides a genome-wide expression profile across diverse neuron types and species [48], Patch-seq combines scRNA-seq with patch-clamp recordings. This method simultaneously captures RNA sequencing, electrophysiological, and morphological data from the same neuron, providing data at an unprecedented resolution. This offers a novel approach to understanding neural computation at the molecular level. Previous work has performed unsupervised analysis of Patch-seq datasets to generate a list of genes that correlate with electrophysiological or morphological properties [6]. However, this approach typically limits the analysis to correlations between individual genes and features of interest, making it less likely to capture the complex interactions between genes and provide a causal explanation of the underlying mechanisms.

To accurately predict electrophysiological features from transcriptomic data without overfitting to region-specific genes, we adapt a comprehensive approach that considers the broader network of gene interactions in addition to gene-feature correlations. We started with one important feature of single neurons: firing rate adaptation [56]. This feature was first discovered in [37], describing how neurons modulate their output to the same input. It is important in various cognitive functions that have been validated by experimental and theoretical works alike: sensory processing from vision [8], audition [57], and olfaction [58]; working memory in language processing [17]; perceptual bistability [46] and multistable perceptions [24]; theta sweep in place cells [13]; precision in spike-timing [28]; and processing of temporally dispersed information [43]. Interestingly, different cell types show large differences in the firing rate adaptation [50]. Parvalbumin (PV) interneurons (IN), recognized by their signature narrow action potential (AP) waveform, show no or little firing rate adaptation. Somatostatin (SST) INs, which shared the same origins from medial ganglionic eminence as PV INs [60], in general have a broader AP waveform and a stronger adaptation compared to PV. PV and SST are widely distributed in the layers and regions of the cortex and account for about 70% of the total INs of the whole cortex [50], although some variability between cortical areas have been reported [49]. These features make them ideal first targets for studying the mechanisms behind firing-rate adaptation.

In previous work, though, the mechanisms underlying firing-rate adaptation were mostly studied in pyramidal cells [1]. In general, when a cell fires an AP, it activates high-voltage activated calcium (Cav) channels. It introduces Ca^{2+} influx, which in turn activates small conductance calcium-activated potassium (SK) channels that generate outward afterhyperpolarization potential (AHP), slowing down the regeneration of incoming APs. However, little is known about whether the mechanism generalizes to INs. In addition to the SK pathway, other mechanisms may also contribute, including M-type K channels, calcium buffer system, and cation (H) current [21].

Here, we utilize the open Patch-seq dataset [20] recorded from primary visual cortex (V1), where both electrophysiological and transcriptomic data are available for PV and SST cells, to search for

transcriptomic correlates of firing-rate adaptation. We first show that firing rate adaptation, measured by the degree of adaptation (dAdap), is a key feature in distinguishing PV and SST cells. We further find that the AP half-width (HW) and dAdap are highly correlated at the single-cell level. Next, we seek the transcriptomic correlation of adaptation using the known transcriptomic correlation of HW as a control. We develop a method to systematically de-noise the original Patch-seq data at the transcriptomic-defined subtype (T-type) level and further validate that HW differences correlate with the corresponding de-noised transcriptomic data. We hypothesize that the SK channel encoding gene should correlate with dAdap, but we surprisingly find that the data does not support this. Instead, the upstream Ca influx-related mechanisms, namely HW and Cav channel encoding genes, can explain the observed dAdap differences. We further predict other genes that are likely involved in modulating firing-rate adaptation. We extend our analysis to a M1 mouse Patch-seq dataset that includes pyramidal cells [44], and an electrophysiological dataset along with a transcriptomic dataset [12] that both cover the same three brain areas from macaque monkeys, confirming the generality of our conclusion. Finally, we built a Hodgkin-Huxley-type model that includes Ca^{2+} dynamics. The model successfully reproduces the observed experimental data and generates testable pharmacological predictions.

2 Results

2.1 Firing Rate Adaptation and Spike Width are correlated in PV and SST Interneurons

PV and SST INs together account for about 70% of the total INs of the whole cortex [50]. Here, we analyze the electrophysiological features of PV and SST cells from the open Patch-seq dataset from the mouse V1 [20]. PV cells show little adaptation over a 1s-long square-pulse injection current, while SST cells show strong adaptation. Furthermore, PV cells show the signature narrow AP waveform, while SST cells show a wider AP waveform (Figure 1A).

We quantitatively measured the firing-rate adaptation by degree of adaptation (dAdap). To do so, we first fit the curve of the instantaneous firing rate to an exponential decay function $f(t) = a + b\exp(-ct)$. After fitting, we compare the firing rate at the end of the $1s$ simulation to the initial firing rate $\text{dAdap} = 1 - f(1)/f(0)$, which varies little at high injection current (above 1.5× rheobase, Figure 1A, 3rd column). In the following, we use the closest sweep to twice the rheobase to measure the dAdap for each cell. We quantify the AP waveform by HW, the average time above half of the peak, and the firing threshold for each AP (see Methods).

Next, we investigate how effectively HW and dAdap can distinguish PV and SST cells, compared to other classification methodology. In [20], PV and SST cell types are defined through a muli-gene classification algorithm. Using this as the ground truth, both HW and dAdap demonstrate high accuracy in distinguishing PV and SST cells (Extended Data Table 1). When combined, a trained classifier achieves an accuracy of 95.3% (Figure 1B). Conventionally, classification is performed using marker genes, such as *Pvalb* and *Sst*, like through immunohistochemistry labeling. To compare the effectiveness of multi-gene classification and single marker gene classification, we analyzed the marker gene distribution in the V1 dataset (Extended Data Figure 9A). Assuming a threshold at the 20th percentile of *Pvalb* and *Sst* counts per million (CPM) distribution to determine whether a cell is *Pvalb*+ or *Sst*+, respectively, we identified a significant population of *Pvalb*+/*Sst*+ cells, resulting in an 89.6% agreement with the multi-gene classification (Extended Data Figure 9A). This suggests that a classifier based on HW and dAdap is better aligned with the multi-gene classification than one based on the conventional marker genes. In addition, we did not find a significant difference in classification accuracy when considering laminar differences (Extended Data Figure 9B). Moreover, our trained classifier from V1 achieves a 86.4% accuracy on a PV/SST dataset collected from L2/3 of the somatosensory area in mice (Extended Data Figure 9C).

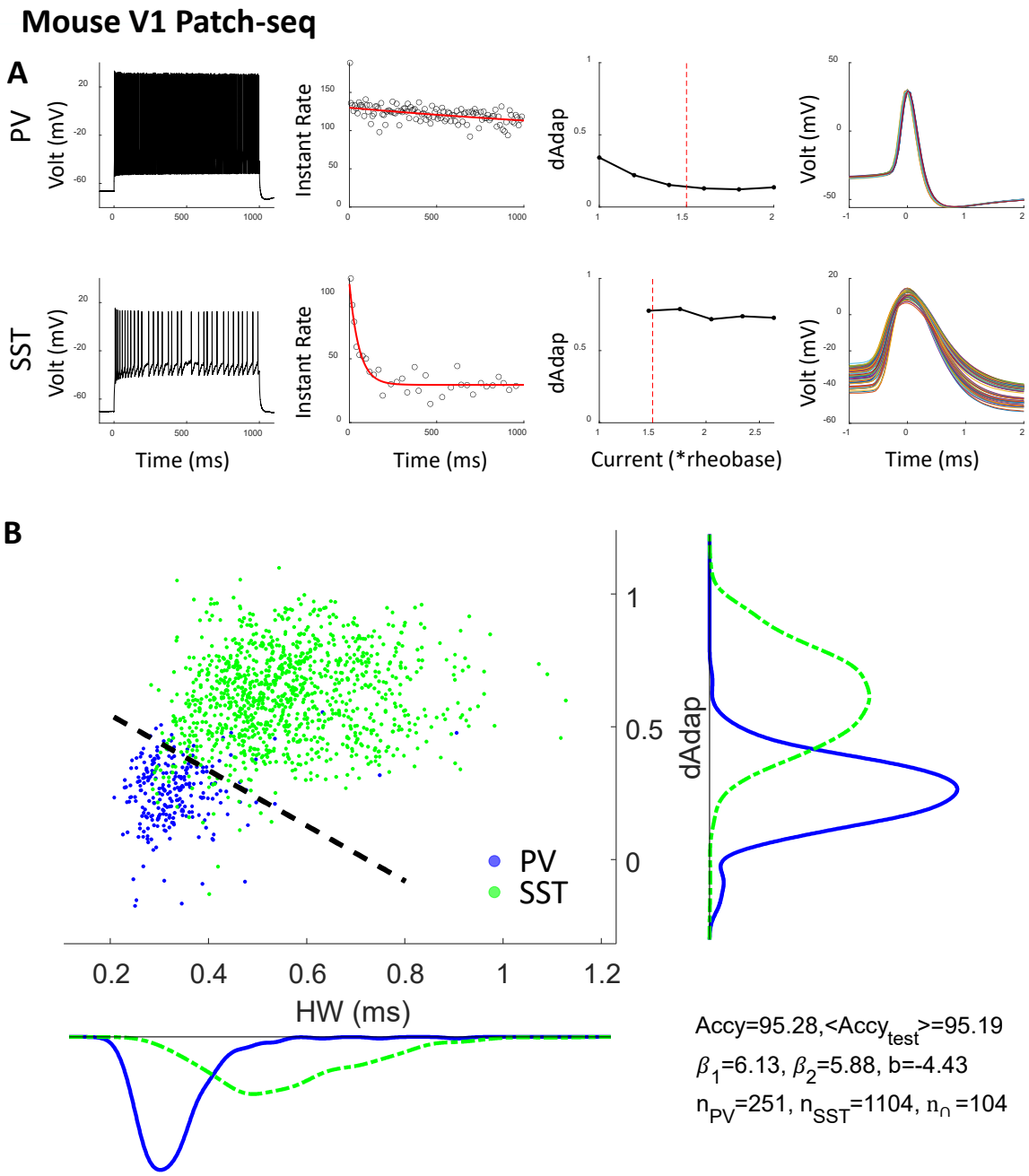

Fig. 1 The degree of adaptation and the width of the action potential are highly correlated. (A) Different electrophysiological features from PV and SST INs. From left to right: one recording over a 1s-long square-pulse current injection. Instantaneous firing rate as one over interspike intervals. The curve is fitted to an exponential decay function. dAdap over injection currents. The red dashed line indicates 1.5× rheobase current. AP shapes are overlaid, while each line represents an AP from the PV cells. Top, results from an example PV cell; Bottom, an SST cell. (B) PV and SST cells can be classified based on HW and dAdap. The dashed line is the classification boundary trained by a Support Vector Machine, which is indicated by $y = -(x\beta_1 + b)/\beta_2$. See supplementary table 1 for details. Accy, classification accuracy, tested accuracy $<$ Accy$_{test}$ $>$ is calculated by the average performance if trained on a randomly split 80% training dataset and tested on the remaining 20% testing set. The sample sizes of PV cells, SST cells, and both *Pvalb*+/*Sst*+ cells (see the main text) are indicated by n_{PV}, n_{SST}, and $n_{\cap}$.

2.2 HW differences are reflected in the transcriptomic data.

Since HW and dAdap are significantly different between PV and SST populations, we next ask what mechanisms might explain these differences and whether these mechanisms can be reflected in transcriptomic data. We start our investigation by performing quality control (Figure 2A, B). We only include cells with high total raw counts (count number) and unique sequenced genes (feature number). In addition, contamination from nearby microglia cells may remain in the data collected by Patch-seq [51]. Following the methodology from [51], we calculated the contamination score for each cell and excluded the cells with high contamination scores (Figure 2B, see Methods). Similar threshold values within a reasonable range would yield qualitatively similar results (Extended Data Figure 10). About 35% of cells remain after all quality controls. We further exclude genes with low expression levels (see Methods). In the following figures, if more genes are in a gene family of interest but not shown in the analysis, it is because those genes failed quality control.

Previous work has shown that HW is controlled by the voltage-gated K^+ Kv3 channel and the Na^+ channel (Nav) in the INs [42, 22]. Specifically, a larger Kv3 conductance leads to faster repolarization after each spike, resulting in a narrower AP waveform and a smaller HW. Similarly, the Nav conductance also contributes through the speed of depolarization. Thus, we expect higher expression of Kv3 and Nav encoding genes to be associated with a smaller HW.

At the single-cell level, increased expression of *Kcnc1*, which encodes Kv3.1, is associated with a smaller HW (Figure 2C) with considerable variability. Particularly, some cells may have a low expression of *Kcnc1* but appear as zero due to the dropout issue, where no RNA copy is detected. To enhance the signal and mitigate dropout issues, we aggregate cells into the transcriptomic-defined type (T-type) level to improve the signal. These T-types are defined by unsupervised clustering on all the genes, exhibiting consistent electrophysiological and morphological properties ([20]). The weighted linear regression (WLR) at the T-type level shows strong significance (Figure 2D, $p = 1.9 \times 10^{-10}$) between *Kcnc1* and HW. Similarly, *Scn1a*, which encodes Nav1.1, also significantly correlates with HW (Figure 2E). These results agree with previous literature [42, 22] and validate our methodology in detecting correlates between electrophysiology features and transcriptomic data.

2.3 Upstream Ca^{2+} influx-related mechanisms may explain the dAdap differences, not downstream SK channels.

After validating our methodology in the HW-related genes, we examine the dAdap-related genes. Firing rate adaptation is commonly attributed to the medium timescale afterhyperpolarization current (mAHP) that is mediated by the Ca-activated K channel, also known as the small-conductance-K (SK) channel [1]. These SK channels, activated by the accumulated Ca through APs, slow down the firing, leading to firing rate adaptation. Thus, we hypothesize that, similarly to the HW case, *Kcnn* family expression should significantly correlate with dAdap. Surprisingly, we do not observe a significant correlation between dAdap and the *Kcnn2*, which encodes a SK channel (Figure 3A).

To understand this discrepancy, we re-examine our data. HW and dAdap are significantly correlated across T-types of SST and PV cells (Extended Data Figure 11A). In addition, [16, 29] (re-analyzed in Extended Data Figure 11B) showed that modulating HW by Kv3.2 knockout or tetraethylammonium (TEA), which inhibits Kv3 gene family, also modulates firing rate adaptation. These observations suggest an alternative hypothesis to explain the observed dAdap differences through transcriptomic data.

Namely, even though downstream SK conductances are the same across PV and SST, their activation may be influenced by the amount of Ca influx through each AP (Figure 3B). This calcium influx is determined by the conductance of Cav channels and the time window during which these Cav channels are activated. The former can be quantitatively measured by HW, while the latter should be reflected by the corresponding gene expressions.

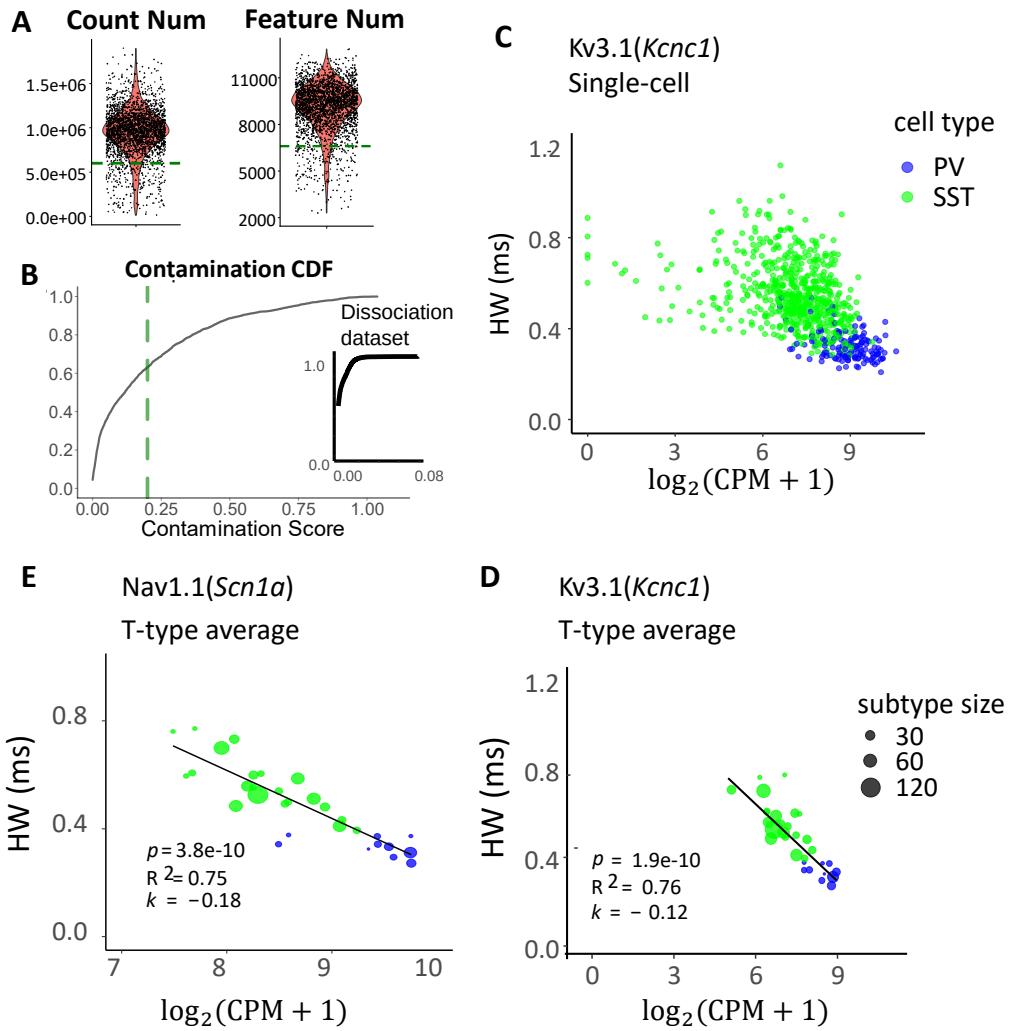

Fig. 2 Normalization of the transcriptomic data and validation in HW-related mechanism. (A) Quality control of Patch-seq V1 scRNA-seq data. The dashed lines indicate the cutoff of total gene count and unique sequenced genes per cell, which are 6×10^5 (left) and 6600 (right). (B) Cumulative distribution function (CDF) of the microglia contamination score. We excluded highly contaminated cells with a score greater than 0.2 (dashed line). The inset shows the CS curve calculated from a dissociated-based dataset [62]. Note that for all cells, CS < 0.08. (C) Scatter plot of HW and Kcnc1, which encodes Kv3.1 channel, expression among V1 PV and SST cells at single-cell level. (D) Bubble plot for the T-type Average of the data in (C). See Methods. The size of the dots represents the sample size of the corresponding T-type. The solid line show the result of weighted linear regression (WLR). p: p-value; R^2: variance explained by the fitting. k: the slope of the fitted line. (E) Bubble plot for weighted correlation between HW and *Scn1a*.

To test this, we look at all the relevant genes in the hypothesized pathway and extract the corresponding p-value from the weighted linear regression (WLR), as we did in Figure 2D, E. Each arrow represents a gene in Figure 3C, D. The x-axis of the arrow represents the significance level of this gene correlated with HW (Figure 3C) or dAdap (Figure 3D) in the WLR. The dashed line indicates the significance at $p = 0.01$. Each arrow starts at the expression level of the PV subtype and ends at the SST subtype. A thicker arrow represents a greater differential expression between PV and SST. The significantly differentially expressed genes are represented by solid arrows (also see Extended Data Figure 12A). The $lg(p^{WLR})$ strongly correlates with the explained variance R^2 at the T-type level (Extended Data Figure 12B).

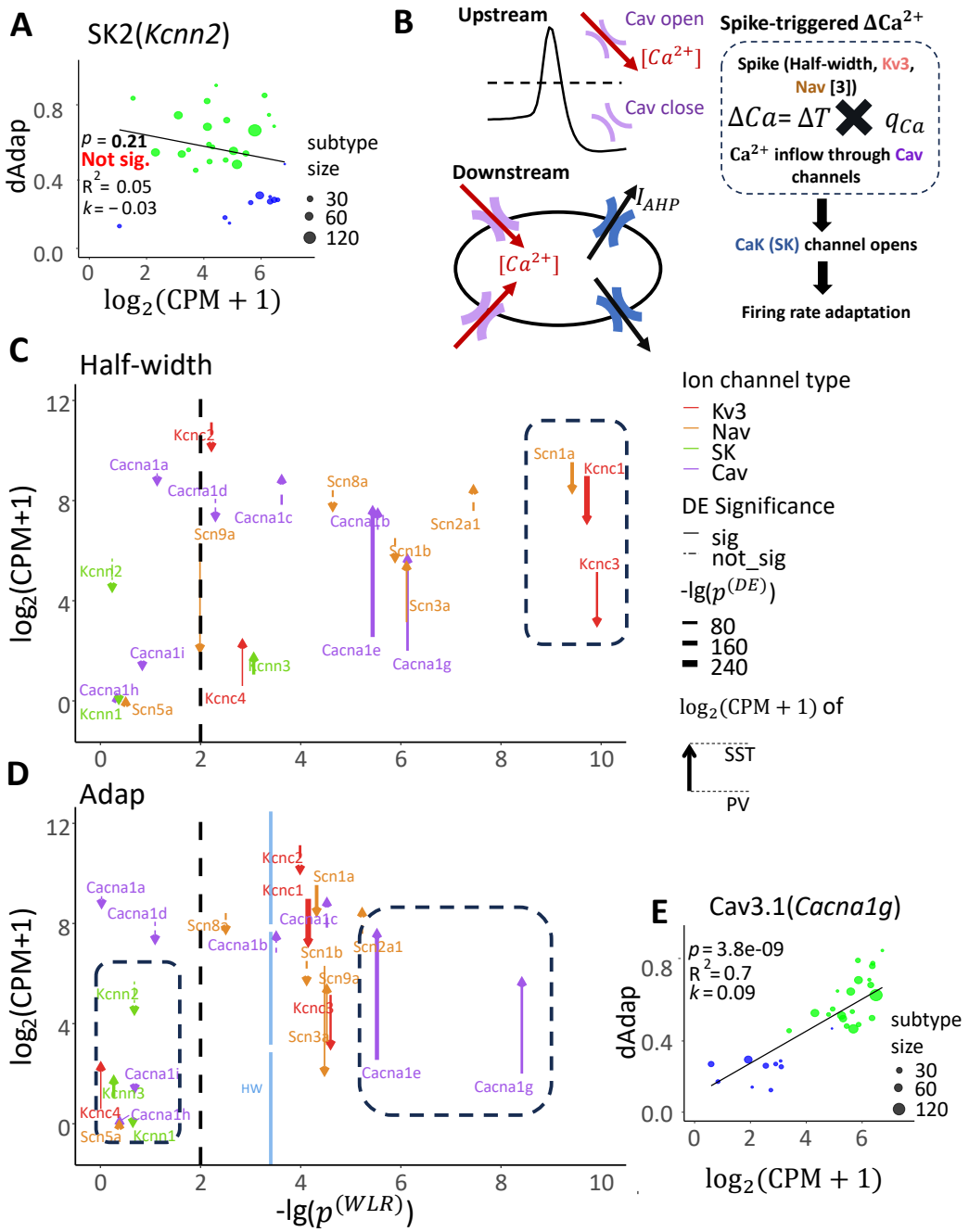

In Figure 3C, within all genes interested, we confirm that *Scn1a*, *Kcnc1* and *Kcnc3* (boxed genes) are the most significantly negatively correlated with HW differences between T-types and are the most differentially expressed genes (DEG) between PV and SST INs, confirming existing experimental findings [42, 22]. Interestingly, not all the highly expressed Kv3 and Nav channel encoding genes (*Kcnc2*, *Scn8a*, *Scn1b*, *Scn2a1*) are DEGs between PV and SST. This highlights that a gene can be functionally important in controlling the HW but does not contribute to HW differences across cell types.

Fig. 3 Downstream SK genes are not significantly correlated with dAdap, but upstream Ca^{2+} influx-related genes do. (A) Bubble plot for weighted correlation between dAdap and *Kcnn2*. The correlation is not significant. (B) Scheme of mechanism for spike frequency adaptation. During each AP, the Cav channels are activated, where the time window is quantified by HW. The activation of Cav channels triggers a Ca^{2+} influx, which increases intercellular Ca^{2+} concentration that activates the SK channel and generates the downstream outward AHP current that leads to the adaptation. (C) Each arrow represents one gene. The x-axis shows the significance of correlation to the HW or dAdap, quantified by WLR. The y-axis shows the normalized gene expression level. The arrows start from the averaged CPM of all PV INs and point to that of SST INs. Up arrows indicate a positive correlation between the gene expression and the HW, and *vice versa*. Arrow width corresponds to the $-\lg(p^{(DE)})$ of the genes differential expression analysis result between PV and SST. Solid arrows represent the genes differentially expressed between PV and SST (DE analysis $q < 0.05$ and log_2(Fold Change) ≥ 1). The vertical black dashed line represented the significance level $p^{(WLR)} = 0.01$. The colors of the arrows label the type of ion channel encoded by the gene. (D) Same as (A) but for dAdap. The dashed blue line shows the significance of the correlation between dAdap and HW ($p^{(WLR)} = 4e - 4$). (E) Correlation between dAdap and *Cacna1g*.

Previous work has suggested that firing rate adaptation is mainly controlled by SK channels [1]. However, all SK channel-encoding genes are not significantly correlated with dAdap differences (genes in the left box in Figure 3D). In contrast, the HW (Extended Data Figure 11A, the blue line in Figure 3D) and HW-related genes (Extended Data Figure 12C, D) and some Cav encoding genes (Figure 3E and Extended Data Figure 12E, boxed in Figure 3D) are significantly correlated with the dAdap difference. Noticing that the Kv3 and Nav genes are more significantly correlated with HW than with dAdap, while the Cav genes are more correlated with dAdap (Figure 3C, D), these genes may not be merely marker genes without functional roles. These results suggest that downstream SK channels may exist in the PV INs as in the SST INs but may not be equally activated because of low Ca influx through each AP.

In addition, the expressions of some genes are more correlated with each other across IN T-types (Extended Data Figure 12F), suggesting they may form a functional group together [19]. Since some genes are highly correlated, we should be able to predict HW or dAdap with fewer genes without losing prediction accuracy. This is confirmed in a statistical model (Extended Data Figure 12G), where we can predict HW using five out of eight significantly correlated genes (DEGs with $p^{(WLR)} < 0.01$, genes located to the right of the dashed line in Figure 3C). Similarly, we can predict dAdap using *Cacna1g* out of seven significantly correlated genes. Importantly, we can predict dAdap based on only HW and the gene *Cacna1g*, without any gene encoding SK channels, suggesting the upstream Ca^{2+} mechanisms control the dAdap differences, but not downstream SK channel conductance.

2.4 Unsupervised filter implies genes that may contribute to the dAdap differences

Beyond the specific genes related to our hypothesized mechanisms, other genes may also modulate dAdap. To explore the identity of these genes, we checked what are DEGs between PV and SST IN and whether they are significantly correlated with dAdap or HW (Figure 4A, see Method). In total, 452 DEGs are significantly correlated with dAdap. Among them, 360 genes are also significantly correlated with HW, while 92 are not. We further checked the fold change and the false discovery rate for these 452 genes (Figure 4B). The positive fold change means gene expression is higher in SST than in PV INs. Based on our hypothesis, these 360 genes (blue points in Figure 4B) may impact dAdap through modulating the upstream Ca^{2+} flux time window, reflected in the HW differences. The remaining 92 genes likely contribute to dAdap through modulating the Ca^{2+} flow rate or the efficacy for Ca^{2+} that activates SK channels. However, we can not fully rule out the possibility that these genes are merely marker genes that distinguish PV and SST cells, such as *Pvalb* and *Sst*. We further perform a gene ontology enrichment study on these 452 DEGs (Extended Data Figure 13), which shows those genes aggregated on the ion transmembrane transporter activity, especially on K^+, Ca^{2+} and Na^+ ion channels, agreeing with our hypothesis.

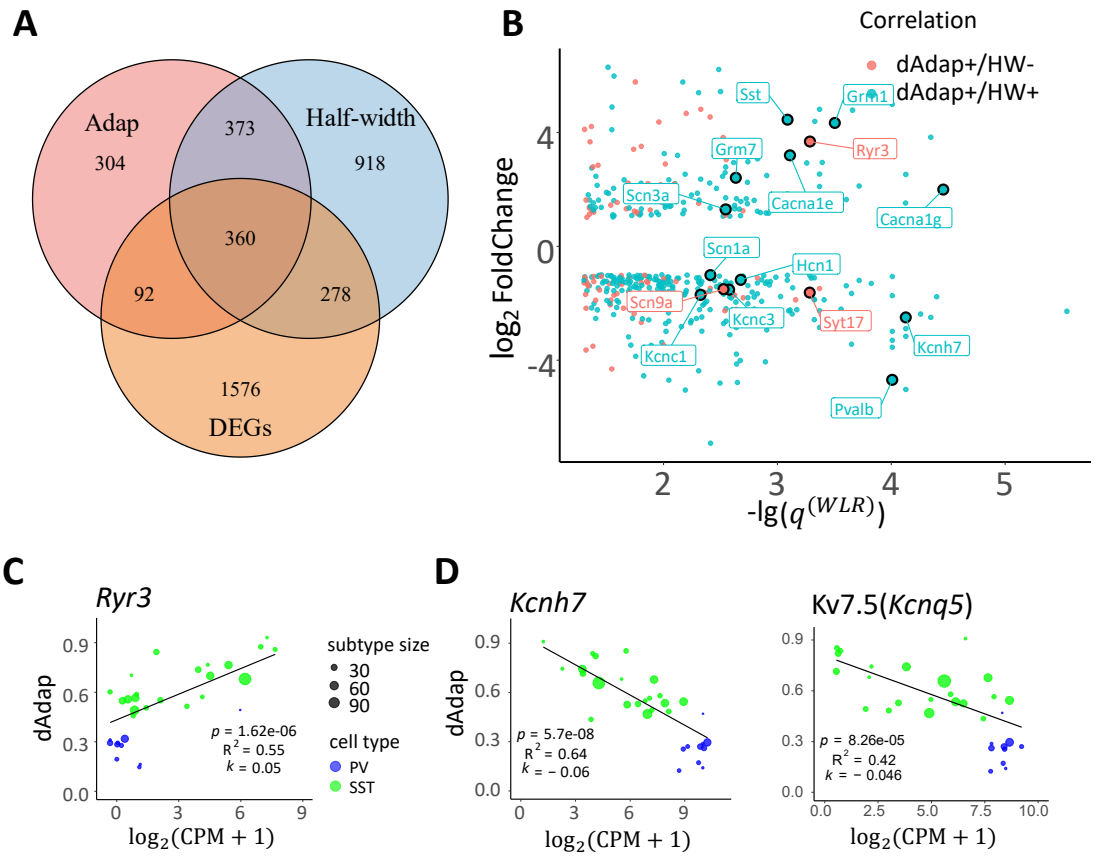

Fig. 4 Lists of genes generated by the unsupervised filter algorithm. (A) Venn plot of Adap highly-correlated genes (pink), HW highly-correlated genes (blue) and differential expression genes (DEGs, in orange). (B) Performance in differential expression analysis and WLR with dAdap for genes in the intersection part of the Venn plot. DEGs that are highly correlated with both Adap and HW are labeled in blue, and DEGs that are only highly correlated with Adap but not with HW are labeled in pink (C) Correlation between Adap and *Ryr3* expression at T-type level. (D)dAdap and *Kcnh7* or *Kcnq5*.

Within the resulting gene list (Figure 4B), we found our hypothesized genes *Kcnc1*, *Kcnc3*, *Scn1a*, *Cacna1e*, *Cacna1g*, validating the reliability of our unsupervised filter. Furthermore, type 3 ryanodine receptor encoding gene *Ryr3* expression is significantly higher in SST cells (Figure 4C), positively correlated with dAdap but not HW. It was suggested a higher *Ryr3* expression can enhance the Ca^{2+} releasing from intracellular storage [7], which may activate downstream SK channels. Furthermore, we find several K channels encoding genes, *Kcnh7*, *Kcnq5*, and *Kcnip2* (Figure 4D, Extended Data Figure 14B) are significantly highly expressed in PV cells, negatively correlated with HW and dAdap. They may contribute to modulating the excitability of INs [14]. Among them, *Kcnq5* encodes the M-type K^+ channel and was suggested to contribute to firing rate adaptation in CA1 pyramidal cells [21]. However, if the M-type K^+ channel were the primary contributor to dAdap, a higher *Kcnq5* expression would be expected to correlate with a greater dAdap. This is contradicted by the data, which shows that PV neurons have higher *Kcnq5* expression but smaller dAdap (Figure 4D). Last, SK channels are impacted by accessory subunits calmodulin, protein kinase CK2, and protein phosphatase 2A [1]. Since the corresponding genes (*Calm1* to *3*, *Csnk2a1*, *Csnk2a2*, *Csnk2b*, *Ppp2r1a*, *Ppr2r1b*, *Ppp2ca*, *Ppp2cb*) are uniformly expressed across PV and SST INs (i.e., they are not DEGs, see the

supplementary table 4), these factors may not contribute in explaining dAdap differences across cell types.

Other potential genes of interest include *Grm1*, which encodes a group I metabotropic glutamate receptor, known to facilitate intracellular calcium release, and *Syt17*, which may enable Ca^{2+} ion binding activity (Extended Data Figure 14A). The H-current-encoding gene *Hcn1* is significantly differentially expressed between PV and SST, but the fold change is close to one. Since the H-current is activated through hyperpolarization, it may not regulate HW or dAdap when the neurons are mostly depolarized. In addition, BK channels can contribute to the regulation of HW and dAdap (Extended Data Figure 14C, D), which agrees with [5], [47].

2.5 Validation in an M1 Patch-seq dataset

We next asked how general our hypotheses can be validated in other brain areas. We analyze another Patch-seq dataset from mouse primary moter cortex (M1), of which electrophysiology features are recorded at room temperature [44]. A significant correlation between HW and dAdap is observed (Figure 5A).

Next, after a similar quality control (Figure 5B) and differential expression (DE) analysis (Extended Data Figure 15A), we showed qualitatively similar results to the V1 dataset by analyzing which genes are significantly correlated with HW or dAdap, and are DEGs simultaneously (Figure 5C, D). The HW is correlated with confirmed *Kcnc1*, *Kcnc2*, *Scn1a*, while dAdap was correlated with the same HW-related genes and Cav genes, *Cacna1g* and *Cacna1e*, but not with the SK genes, *Kcnn1* to *Kcnn3*. In addition, we observe that *Cacna1e* (Cav2.3, R-type) is significantly correlated with both HW and dAdap. Example correlations between genes and HW or dAdap are shown in Figure 5E to G, and Extended Data Figures 15B, C. These results supported the upstream Ca^{2+} related mechanisms control the dAdap differences across cell types in M1 as well.

However, when considering HW and dAdap differences within interneurons and pyramidal cells, different mechanisms may exist, known as the class-driven effect [6]. For example, *Kcnc1* explains HW differences across excitatory (E) and inhibitory (I) cells as a whole population (Figure 5E), but it can only explain the HW differences of IN but not pyramidal cells (Extended Data figure 15E, $p_I < 0.05, p_E > 0.05$). We quantified the class-driven effect by the significance of an interaction term in a statistical model, following [6] (See methods). Indeed, the class-driven effect is significant for *Kcnc1* in explaining HW differences (Extended Data figure 15E, $p_{class} < 1e-3$). This effect is also observed in some Nav and Kv3 encoding genes (Extended Data figure 15D. The full list is in the supplementary table 6). This effect is less common in Cav and SK encoding genes. Only *Cacna1g* shows a marginal significance $p_{class} = 0.049$ of class-driven effect in explaining dAdap. These suggest that the mechanisms that control the HW of pyramidal cells may differ from those of INs, but the mechanisms in controlling Ca^{2+} influx rate and SK channels may be similar in both cell classes.

We further explore what mechanism can control the HW differences of pyramidal cells. None of the Kv3 genes can explain the observed differences in HW within pyramidal cells (Extended Data Figure 16A). Alternatively, HW may be controlled by BK channels in pyramidal cells [47], [5]. However, our data do not show a negative correlation between BK genes (Extended Data Figure 16B, C). Combined with a more serious dropout issue when the expression level is low (Extended Data Figure 16A, C), we suspect that the signal is covered by the large noise for those genes, making it hard to detect.

2.6 Regional transcriptomic and electrophysiological differences across macaque monkey brain regions

To determine if our hypothesis extends beyond specific cell types and brain areas and generalizes across species, we analyze one electrophysiological dataset and one transcriptomic dataset from macaque monkeys, covering the same three brain areas: V1, lateral intraparietal area (LIP), and prefrontal cortex (PFC). The HW and dAdap are measured as before (Figure 6A, B). We first show a significant

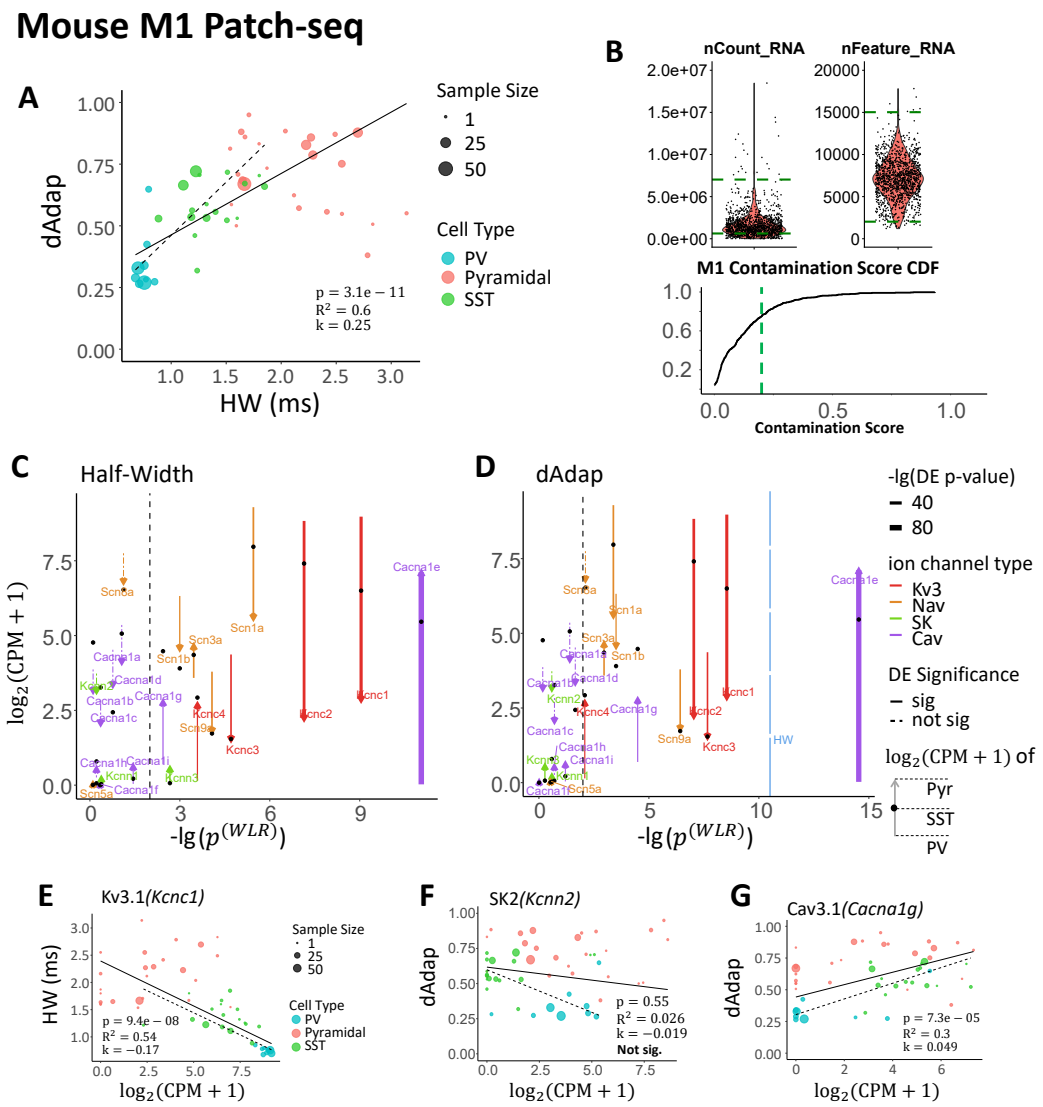

Fig. 5 Validation in a mouse M1 dataset. (A) Correlation between HW and dAdap at the T-type level from the mouse M1 dataset. The dashed line indicates the fitting for only PV and SST INs. (B) Quality control for feature number, total gene count, and quality control for contamination. (C, D) Arrow plots of HW and dAdap as in Figure 3. Each arrow represents one gene, starting from the averaged expression of PV and pointing to that of pyramidal cells. The black dots indicate the expression of SST. (E) Correlation between *Kcnc1* at the T-type. The dashed line indicates the fitting only for PV and SST INs. (E) Correlation between *Kcnn2* and dAdap. The fitted slope is not significantly positive. (G) Correlation between *Cacna1g* and *dAdap*.

correlation between HW and dAdap across individual cells collected from different brain areas (Figure 6C). Within each region, HW and dAdap are consistently smaller in INs compared to excitatory cells. Across brain regions, HW shows an increasing trend for pyramidal cells, while HW and dAdap are significantly higher in PFC than in V1 for INs.

We next asked whether these differences may be explained by the transcriptomic data from [12] through similar mechanisms, where the data is collected from the whole brain using unique molecular identifier (UMI) sequencing and further clustered into cell types. We further calculate a trimmed mean for each subtype at each brain region. Similar gene differences are observed in macaque PFC, LIP,

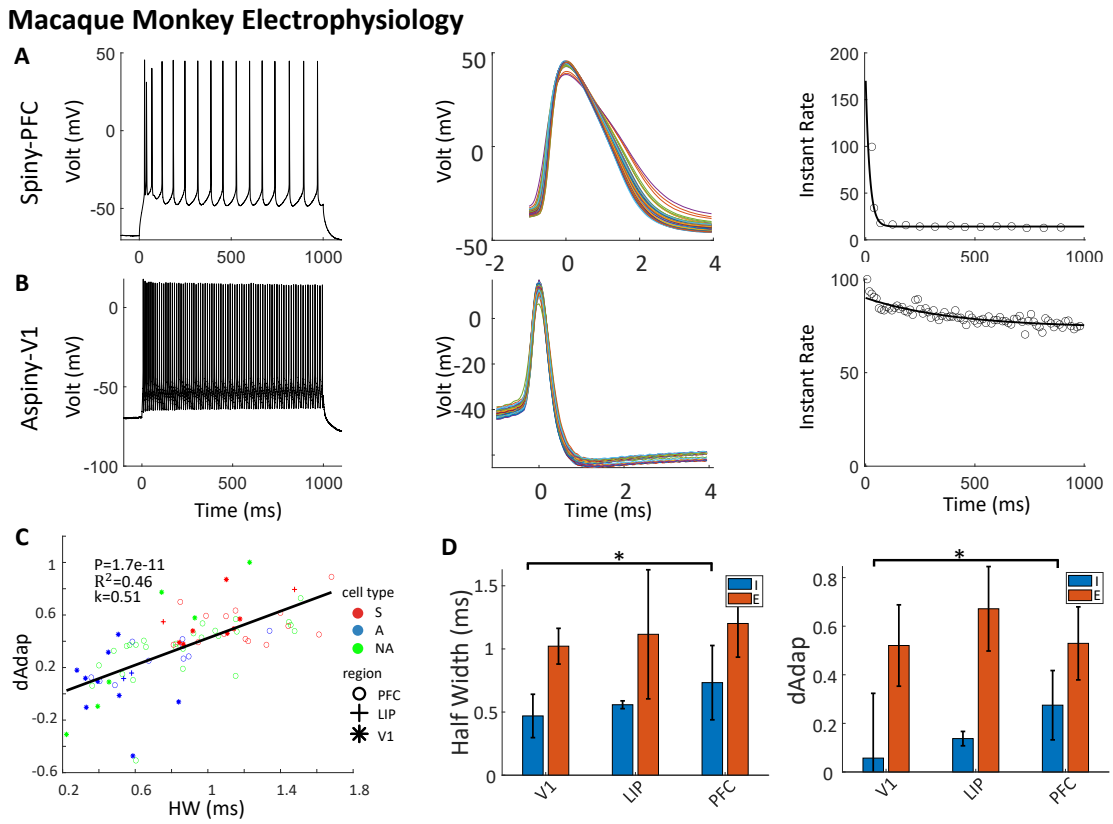

Fig. 6 Cell type and regional differences in macaque monkey datasets. (A) Different electrophysiological features from a PFC spiny cell, presuming a pyramidal cell. From left to right: recording over 1s-long square-pulse current injection; AP waveform; instantaneous firing rate as one over interspike intervals. (B) Same as (A) but from a V1 aspiny cell, presuming an interneuron. (C) Correlation between HW and dAdap in a single cell from the multiregional monkey dataset. Cell types are determined by cell morphology. A: aspiny, supposing INs; S: spiny, supposing excitatory pyramidal cells; NA: not applicable. Different symbols indicate where the recorded cells are located. $N = 77$. (D) Regional HW (top) and dAdap (bottom) differences in the macaque monkey dataset. *: PFC have significantly wider AP and stronger firing rate adaptation than V1 for INs, $p < 0.05$. $p_{HW} = 0.0312$, $p_{dAdap} = 0.0377$. $N_I^{V1} = 9$, $N_E^{V1} = 7$, $N_I^{LIP} = 2$, $N_E^{LIP} = 2$, $N_I^{PFC} = 10$, $N_E^{PFC} = 14$.

and V1, compared to mouse V1 data (Figure 3, Extended Data Figure 17). For example, the HW differences can be reflected by the KCNC1 and SCN1B in general, while the class-driven effect is also observed (Figure 7A). The dAdap differences again are not reflected by the downstream KCNN2 gene but by the upstream CACNA1E gene (Figure 7B). This suggests that the mechanisms to explain HW and dAdap differences may be conserved between mice and macaque monkeys.

When comparing across regions (Figure 7C), for pyramidal cells, *Kcnc1* and *Scn1a*, *Scn1b* all showed a significant decrease, agreeing electrophysiology which showed a wider HW in the PFC. Noticing the fold change of *Scn1a*, *Scn1b* is much larger than that of *Kcnc1*, we hypothesize the regional differences of HW from pyramidal cells mainly result from the change of Na^+ channels but not K^+ channels. Interestingly, M-type encoding genes, SK encoding genes, and Cav encoding genes all show an increasing trend. Combined with a wider HW, our hypothesis suggests that there should be a stronger firing rate adaptation, a result that is not reflected in the electrophysiology data. The reason for that will require further study, ideally on a Patch-seq dataset collected from macaque monkey PFC.

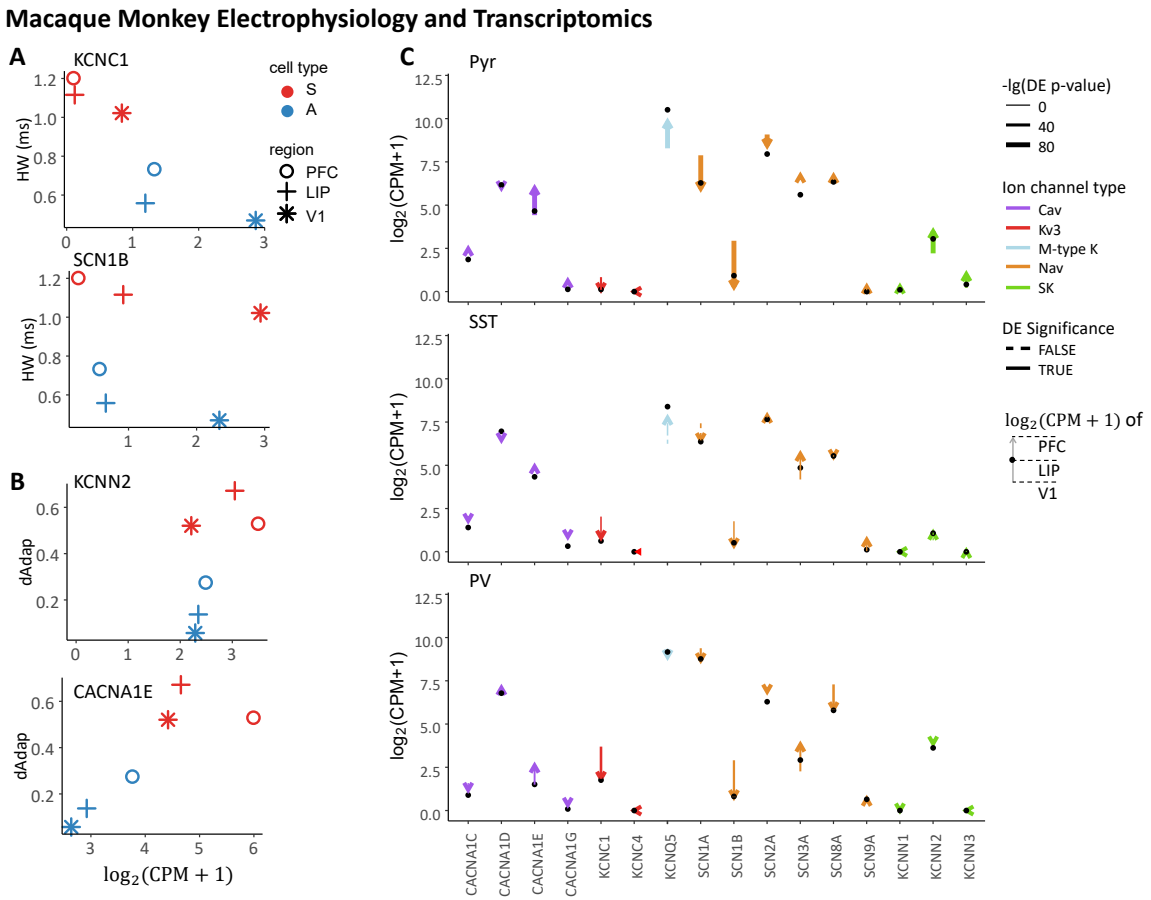

Fig. 7 Cell type and regional differences in macaque monkey datasets. (A) the relationship between HW and expression KCNC1 and SCN1B across cell types and regions. A: aspiny, supposing INs; S: spiny, supposing excitatory pyramidal cells. Different symbols indicate where the recorded cells are located. (B) same as (A) but for the relationship between dAdap and KCNN2, CACNA1E. (C) Transcriptomic data differences from pyramidal cells (top), SST (middle), and PV interneurons across different brain regions. Each arrow represents one gene, starting from the trimmed mean in V1 and pointing to that in LFP. The black dot on the arrow indicates the trimmed mean in LIP. The significance is indicated by solid arrows with DE analysis $q < 0.01$ and $|log_2(\text{Fold Change})| \geq 0.4$. $N^{V1}_{Pyr} = 2.1e3$, $N^{V1}_{PV} = 1.3e3$, $N^{V1}_{SST} = 1.1e3$, $N^{LIP}_{Pyr} = 6.0e3$, $N^{LIP}_{PV} = 571$, $N^{LIP}_{SST} = 509$,$N^{PFC}_{Pyr} = 1.3e5$, $N^{PFC}_{PV} = 1.1e4$, $N^{PFC}_{SST} = 8.5e3$.

The INs show a significant increase in HW and dAdap in PFC compared to those in V1. This may come from a cell density change (less PV cells and more SST cells) or cell property changes across regions. The former is less likely, as the density of PV cells consistently represents between 40% to 50% of the total PV and SST population across regions [12] (though, see [49] for different findings). Still, the single-cell property may change unevenly across cell types. In our analysis, the *Kcnc1* and *Scn1a*, *Scn1b* all showed a significant decrease in PV and SST INs, agreeing with a wider HW in the PFC. Also, the Cav encoding genes significantly increased in PFC, but not the SK gene family, supporting the upstream Ca^{2+} influx and contributing to the dAdap increases. Noticing the M-type encoding gene *Kcnq5* increases in PFC, implying it may contribute to the dAdap differences across regions. Interestingly, genes exhibit greater fold changes across regions in PV INs than SST INs, suggesting that the adaptation change in the PV cell population is more pronounced than in the SST cell population. Detailed differential expression analysis across cell types and brain areas is provided in the supplementary data 1.

2.7 A Hodgkin-Huxley model reproduces the upstream effects on the firing rate adaptation

To support that upstream Ca^{2+} influx can impact firing rate adaptation, we built a Hodgkin-Huxley model that reproduced the behavior and generated testable pharmacological predictions. Our model included Nav, Kv, Cav and SK channels that generate AHP (Figure 8A). In addition to the cell voltage, we include the dynamic of Calcium concentration $[Ca^{2+}]$, where the increase of $[Ca^{2+}]$ is proportional to the Calcium current I_{Ca} (see Methods). Our model can successfully reproduce the observed firing rate adaptation (Figure 8B, black line in C).

To illustrate the impact of the upstream mechanism of firing rate adaptation, we modify the conductance of the K channel g_K and the SK channel g_{AHP} in the model (Figure 8C). Reducing g_K decreases the repolarization current, which broadens the AP waveform and increases the HW. A wider AP waveform allows for more Ca^{2+} influx during each AP, leading to a larger dAdap (Figure 8C, blue). This agrees with the experimental observation when modulating the g_K by Kv3.2 gene knock-out or applying Kv3-sensitive TEA (Extended Data Figure 11). In addition to a reduced g_K, reducing g_{AHP} only impacts the SK current, but not the AP waveform. As a result, dAdap decreases, but HW remains the same (Figure 8C, red). This can be tested pharmacologically using SK channel antagonism apamin. In addition, we systematically varied the conductance of the K channel and the Ca channel g_K, g_{Ca} (Figure 8D). The HW is dominantly determined by g_K, but not g_{Ca}, while dAdap increases when g_K reduces or g_{Ca} increases. This supports that the AP waveform is an upstream mechanism to downstream firing rate adaptation, while Ca^{2+} inflow rate has a litter impact on the AP waveform.

Lastly, to reproduce the heterogeneity observed in the V1 INs, we randomly draw g_{Na}, g_K, g_{Ca} from a correlated normal distribution (i.e., covariant between two random variables is not zero, see Method), implied by the data. We qualitatively reproduce the wide-range heterogeneity of HW and dAdap observed in the V1 IN dataset.

3 Discussion

Our analysis explores the potential of linking transcriptomic expression differences to AP shape and firing rate adaptation differences across subtypes, regions, and species. Starting with the mouse V1 Patch-seq dataset, we show that HW differences significantly correlate with the trimmed mean of Kv3 and Nav encoding genes, agreeing with the literature. Importantly, the dAdap differences can not be explained by downstream SK channels but by upstream Ca^{2+} influx-related mechanisms. Namely, the AP shape, quantified by HW, controls the time window of Ca^{2+} inflow during depolarization, and the conductance of Cav channels controls the Ca^{2+} inflow rate. We investigate other potential contributing genes through an unsupervised filtering workflow. Next, we observe a similar correlation in a mouse M1 Patch-seq dataset, including pyramidal cells. We further extend our analysis to macaque monkeys through one electrophysiology dataset and one transcriptomic dataset, where both datasets include V1 and PFC. We showed that INs in PFC have a wider HW and a stronger dAdap, and these differences can be explained by the transcriptomic differences through the same mechanisms. Finally, we build a minimal Hodgkin-Huxley model with Ca dynamics to reproduce the differences in HW and dAdap observed across neurons.

Our work pioneers the use of new transcriptomic datasets to understand important electrophysiological features of neurons across regions and species. Our methodology becomes available only because of improvements in sequencing technologies. So far, the rich transcriptomic datasets are mostly used in distinguishing different cell types and developing downstream gene-editing tools [62, 20, 12, 36]. However, in many scenarios, this line of study is difficult to unravel the intricate functions of individual genes in explaining neural electrophysiological activities. Early work from [52] identifies potential genes by combining transcriptomic datasets with electrophysiological datasets. Patch-seq provides electrophysiological and transcriptomic data from the same cell, providing a unique link at an unprecedented level [33]. Only by utilizing this data in the Patch-seq can we infer the causal links

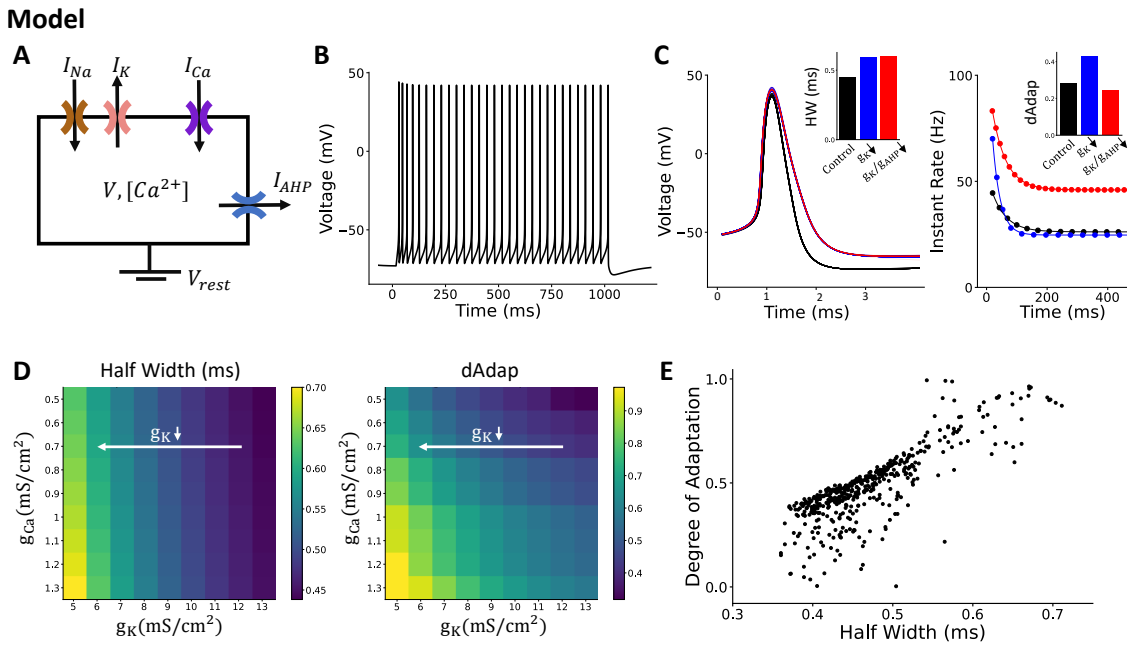

Fig. 8 A Hodgkin-Huxley model reproduces the upstream control of dAdap.(A) Scheme of the model. Our model includes four ion channels. The change of $[Ca^{2+}]$ is proportional to the I_{Ca}. (B) An example trace of the model. (C) AP waveform and firing-rate adaptation in the control case ($[g_K, g_{Ca}, g_{AHP}] = [12, 0.7, 5]mS/cm^2$), reduced g_K ($[6, 0.7, 5]mS/cm^2$), and reduced both g_K and g_{AHP} ($[6, 0.7, 2.5]mS/cm^2$). The insets show the HW and dAdap in these three cases. The HW of three conditions are $[0.451, 0.593, 0.597]$, respectively; the dAdap are [0.280, 0.428, 0.242]. (D) Changing of HW and dAdap over g_K and g_{Ca}. Reducing g_{Ca} only changes dAdap but not HW. The white arrow indicates the black to blue in (C). (E) Varying g_K, g_{Na}, g_{Ca} reproduced the observed distribution of HW and dAdap. The correlation between HW and dAdap is $R^2 = 0.83$.

between gene expression differences and HW and dAdap differences, which can be further tested in other datasets across brain areas and species. We study the firing rate adaptation because of its important role in many functions, such as [8, 57, 17, 46, 13, 28, 43]. Based on our analysis, we can test whether the adaptation differences of INs across brain areas lead to functional differences between sensory areas and prefrontal areas in a model. Further, we can infer the strength of IN adaptation across the brain areas based on the multi-regional transcriptomic database and test their functional role in a large-scale model, similar to [11, 18]. Naturally, our methodology is not limited to the firing rate adaptation but can be applied to understand other important features across brain areas, such as bursting, sub-threshold oscillation, etc.

In analyzing the firing rate adaptation, the most natural hypothesis to explain the differences in dAdap will be differences in SK channel conductance across PV and SST INs since the SK channels mediate the mAHP that leads to the firing rate adaptation [1]. However, we do not find a positive correlation between SK channel encoding genes and dAdap (Figure 3A). Rather, we suggest that upstream mechanisms in the activation of SK channels explain the observed differences (Figure 8). If we only analyzed SK channels, we might suggest that SK channels did not contribute to the firing rate adaptation of INs, which is not the case. Our example shows the importance of considering the gene function comprehensively but not rushing to an inaccurate conclusion.

The upstream mechanisms of SK channel activation depend on the time window and the flow rate of Ca^{2+} through Cav channels. Since the time window, qualified by HW, is larger in SST cells than in PV cells, the Ca^{2+} influx per AP is greater in SST cells, even if the Cav channel conductance is identical. Moreover, we found that *Cacna1g*, which encodes T-type Ca channels, and *Cacna1e*,

which encodes R-type Ca channels, are significantly correlated with dAdap. However, the precise role of these Ca channels remains unclear. T-type Ca channels are activated at low voltage (-60mV) [9], making them unlikely to be involved in AP-triggered dynamics during the depolarization phase. Nevertheless, recent studies show they are at least functionally coupled with SK channels in midbrain dopaminergic neurons [59] and thalamic dendrites [15]. Additionally, a study on rat pyramidal cells [26] demonstrated that nearly all voltage-dependent Ca channels, including T-type, are coupled with downstream mAHP. Another possibility is that T-type Ca channels generate a transient inward Ca current at the onset of the current step, directly contributing to firing rate adaptation in a manner independent of the SK pathway. Conversely, R-type Ca channels are high-voltage-gated [9] and may play a more significant role in regulating dAdap. Our analysis across cell types and regions further emphasizes the potential role of *Cacna1e* in explaining dAdap differences (Figure 5D, Figure 7B, C, Figure 17). However, [26] found that blocking R-type Ca channels had no effect on mAHP recorded at the soma, despite SK channels in the dendrites being tightly coupled with R-type Ca channels in regulating Ca influx. It's important to note that their experimental protocol was limited to inducing mAHP with a single action potential within a 50 ms time window, which may not fully capture the dynamics observed during firing rate adaptation over a 1-second-long stimulation. Additionally, the spatial distribution of these channels may differ between pyramidal cells and interneurons. Further research is needed to clarify the exact dynamics of different Ca channel types.

During our unsupervised analysis of all genes, we found more genes related to intracellular Ca modulation. Among them, Ryanodine Receptor 3 (*Ryr3*) is significantly correlated with dAdap but not HW (Figure 4C), agreeing with the role in regulating Ca^{2+} releasing from intracellular stores [1]. In addition, another modeling study [35] suggested a similar mechanism to explain the adaptation changes in neuropathic pain, supporting that *Ryr3* may contribute to dAdap differences. Other mechanisms that modulate dAdap may be related to the M-type K current [21], which can also be fast activated by depolarization during AP but slowly deactivate below the firing threshold. However, in our analysis, the expression of the M-type K genes (*Kcnq5*) is negatively (Figure 4 D) or not correlated (Extended Data Figure 16H) with dAdap, suggesting that they may not play an important role in explaining differences within a region. However, we cannot rule out their potential role in explaining regional dAdap difference for pyramidal cells since LIP has a larger dAdap and a higher expression of *Kcnq5* (Figure 7C). H-type K current is also suggested to impact mAHP [21] when the cell is depolarized. These H-currents may not impact the firing rate adaptation since the cell was polarized around the threshold during the 1s recording. Interestingly, *Hcn1*, which encodes the H-current, is highly expressed in PV cells (Figure 4B), contradicting reports that the sag current, primarily driven by the H-current, is smaller in PV cells compared to SST cells in both mouse visual areas [32] and the human neocortex [31].

Last, we stress the importance of handling Patch-seq data with extra care. On the side of electrophysiology, the dataset often adopted a uniform recording strategy such that it can be scaled up across different areas of the brain. However, the huge heterogeneous response from different cells can make the relevant features ambiguous. For example, in measuring the degree of adaptation, we observed that only a recording with 1.5× rheobase could be robust (Figure 1B). Since the rheobase of PV INs is much higher than that of SST INs, a uniform protocol that typically goes up to $800pA$ may be sufficient for the measurement of SST INs but not for PV INs. This inevitably leads to biased sampling in our e-feature statistics. Regarding transcriptomic data, we found that careful noise control is crucial in providing interpretation. Since we focus on a few genes, we cannot rely on the large number of gene features the data provided while they are used in the classification studies. To balance that, we use a high threshold for the total number of genes and the number of features, excluding potentially contaminated cells, and analyze at the transcriptomic subtype level. Furthermore, the differences between and across cell classes may come from different mechanisms [6]. One example is *Kcnc1*, of which the class-dependent effect is significant, suggesting different mechanisms from excitatory cells or interneurons. Another limitation in interpreting the regional differences of macaque monkeys is that we use the same hypothesis built from mouse datasets while species differences are not considered. To show

whether the dAdap mechanism is similar across mice and macaque monkeys, a similar analysis of a Patch-seq dataset from macaque monkeys, best at PFC, is needed.

In summary, we find that the transcriptomic data can explain differences in AP shape and firing rate adaptation across cell types and regions. Based on the analysis, we suggest differences in upstream Ca^{2+} influx determine the adaptation differences, but not downstream SK channels. This highlights the need to be cautious in delivering conclusions on single genes. Our methodology can be generalized to render electrophysiological predictions across brain regions by analyzing existing transcriptomic data, opening new directions for both experimental and theoretical studies.

Methods and Materials

3.1 Datasets

The transcriptomic data and electrophysiological data were accessed via Allen Institute for Brain Science's Cell Types Database - Mouse Patch-seq dataset on January 06, 2020 [20]. Electrophysiological recordings were made at physiological temperature (34 °C). This dataset contains 4,284 mouse cells from the primary visual cortex(VISp) layer1, layer2/3, layer4, layer5, layer6a and layer6b. Cells tagged with PV and SST are included in our analysis.

The Patch-seq dataset of adult mouse primary motor cortex (MOp) was accessed from [44]. This dataset collected transcriptomic and electrophysiological data from 1,329 cells at room temperature (25 °C) from mouse MOp layer 1, layer 2/3, layer 5, and layer 6. Cells tagged as PV, SST, and pyramidal (ET, IT, CT, and NP) cell types are included in our analysis.

The electrophysiological dataset from mouse S1 Layer 2/3 was collected from PV-Cre-Ai9 or SST-Cre-Ai9 line as in [23]. Tissue acquisition, processing, and used solutions are described in detail by [39]. The dataset consisted of 16 PV cells and 21 SST cells from 20 individuals of either sex within an age range of 18 days to 35 days.

The macaque monkey transcriptomic dataset, collected through unique molecular identifier (UMI) sequencing, is accessed from [12]. Only the data from monkey No. 2 is used for better area annotation. We exclude the data with ambiguous area annotation, i.e., data from slices across two or more areas. Data from all layers are used.

The intracellular recordings of macaque monkey neurons were obtained in the Inoue and Martinez lab. Tissue acquisition, processing, and used solutions are described in detail by [25]. The dataset consisted of 247 recorded neurons from 11 individuals of both sexes with an age range of 4.39 to 14.6 years.

3.2 Electrophysiological measurements

We use the same measurement as in [38]. We automatically set up a detection threshold to detect an action potential (AP) in any given voltage trace $V(t)$ by the following: We first set up an upper bound as $V_{up} = \min\{\max(V(t)), 0\}$, then a lower bond as V_{low} =median$(V(t))$. Further, we set the detection threshold as $V_{thr} = \max\{0.8V_{up} + 0.2V_{low}, -20\}$. Next, the ith AP is detected at t_i if $V(t_i) < V_{thr}$ and $V(t_i + \Delta t) \geq V_{thr}$, with the resolution in our recordings $\Delta t = 0.05ms$. Furthermore, we exclude any APs within $0.5ms$ following another AP. The rheobase current is the minimum current that triggers an AP in the experiments.

The AP-related properties are calculated from aggregated APs from all the sweeps with less than 40 APs while excluding the first AP in each sweep. The maximum voltage of each AP is calculated from the $2ms$ time window following the trace past the AP detection threshold. The AP threshold is calculated as the voltage when the voltage deviation is $20mV/ms$. The AP half-width is calculated as the time of the AP above the midpoint between the peak and the threshold. To improve precision, linear interpolation is used to calculate the threshold and AP half-width.

The degree of adaptation (dAdap) is extracted from the instantaneous firing (IF) curve. IF curves are calculated as $r(t_i) = 1/(t_{i+1} - t_i)$. Next, we fit the IF curve to an exponential function $f(x) = a + b\exp(-cx)$, using *curve fit* function of *scipy* package in Python. The dAdap is the proportion of the change in firing rate between 0s and 1s. dAdap $= 1 - f(1s)/f(0)$. Due to the large variance of dAdap around the rheobase, we choose the dAdap from the sweep closest to twice the rheobase. If a cell does not have a sweep larger than 1.5× rheobase, we exclude the cell from further analysis.

3.3 Quality control of the transcriptomic data

From the raw counts in the Patch-seq database, we exclude cells whose number of unique sequenced genes is less than 6600 and cells whose total counts are less than 6×10^5 (Figure 2 B, Supplement Figure 15A). Genes sequenced in less than 100 cells were filtered out. Raw counts were normalized by count per million () and then transformed to $\log_2(+1)$. We refer to a dissociated single-cell dataset[62] as the uncontaminated database. Following [51], the contamination score CS describes how much microglial marker genes[30] are presented in the sequenced cells.

Single-cell RNA samples collected by Patch-seq could be contaminated by neighboring microglial cells, but not those collected by dissociated cells

$$CS_{N_M} = \frac{P_{N_M} - D_{N_M}}{D_{M_M} - D_{N_M}}$$

Here, X_{A_M} represents the median of 50 marker genes from the Patch-seq (P) or dissociated (D) dataset of type A in microglial cells. The marker genes differ across cell types (PV or SST IN, pyramidal cell, microglial cell). We adopt the marker gene list for each cell type from [62]. The contamination score CS ranges from 0 to 1, reflecting the excess of off-target marker expression. We limited our analysis to cells with $CS < 0.2$ (Figure 2 C, Figure 5 B)

3.4 Classifier

An exhausted search is applied to train a single-parameter classifier. The value θ classifies PV and SST with the best accuracy is reported. In some scenarios, some cells are excluded from downstream analysis if the classification is ambiguous. To do that, we develop an algorithm that finds the best improvement by losing the minimum number of samples. To do that, a score is calculated based on both the accuracy and remained sample size. Without losing generality, assuming the average value for feature x of PV $< x_P^i >$ is lesser than the value of SST cells $< x_S^i >$

$$N_{right}(\theta_l, \theta_r) = \Pi(x_P < \theta_l) + \Pi(x_S > \theta_r) \tag{1}$$

$$N_{wrong}(\theta_l, \theta_r) = \Pi(x_P > \theta_r) + \Pi(x_S < \theta_l) \tag{2}$$

$$S(\theta_l, \theta_r) = \frac{N_{right} - 3N_{wrong}}{\Pi(x_P) + \Pi(x_S)} \tag{3}$$

where $\Pi(x)$ summarize the number of data point satisfies the condition x. The optimal value pair of θ_l,θ_r is reported for each feature x with the highest score.

For training a classifier based on HW and dAdap, we find the best linear manifold that splits the cells by using the Support Vector Machine algorithm in Matlab. The resulting line is indicated by $\beta_1 x + \beta_2 y + b = 0$. To test the robustness of this method, we randomly split the data points into 80% training set and 20% testing set. We calculate the average performance of 100 repetitions $< \text{Accy}_{\text{test}} >$. To identify cells with low classification accuracy, we employed a Gaussian Mixture Model (GMM). This model assumes that the data from a cell type are generated from a mixture of two Gaussian distributions, calculated by Matlab's *fitgmdist* function. The classification of each data point was based on the highest posterior probability derived from the posterior function, which

computes the likelihood that each data point belongs to each Gaussian component. The curves with 95% posterior probability for each cluster are reported as confidence boundaries.

The fitted parameters are included in the supplementary table 1.

3.5 Multiple linear regression model

To avoid the dropout issue in the scRNA-seq data in weighted linear regression, a gene is excluded if the number of cells it expresses is at least 10% among all the genes.

Each cell in the dataset is associated with a T-type tag. The mean trimmed expression for each T-type is calculated by averaging the expression of individual cells after removing the top and bottom 25% expression.

We used a weighted linear regression to study the correlation between HW or dAdap with different genes. The significance of observing a non-zero slope p, variance explained R^2, and fitted slope k are reported for each pair. When comparing multiple models, correction for the multiple testing problem is necessary. To do so, we adjusted p-values with the false discovery rate (FDR) using the Benjamini-Hochberg method [4]) (Extended Data Figure 12B).

We train the multiple linear regression model to predict HW or dAdap based on genes. We first test the performance of the prediction by including all the significant correlated genes identified in Figure 3.

$$\text{HW } or \text{ dAdap} = \sum \alpha_i g_i + \beta$$

where g_i is the $\log_2$ of a gene, and β is the intercept. The weights α_i are fitted through a multiple variable linear regression. Noticing that we only have 31 T-type (10 PV and 21 SST), the more genes we include, the more likely we observe an overfitting problem. We next adapt the Akaike Information Criterion (AIC) to select the model that could explain the greatest variances with the fewest number of genes [10, 41]. Furthermore, since we hypothesized that dAdap depends on HW, the performance of predicting dAdap using HW and *Cacna1g* is tested.

$$\text{dAdap} = \alpha_1 g_{Cacna1g} + \alpha_0 \text{HW} + \beta$$

The genes and corresponding fitted weights are listed in the supplementary table 3 file.

3.5.1 Regression with respect to Cell Class

To test which genes have a class-driven effect in explaining HW or dAdap, we fit a class-driven linear model as in [6]:

$$\text{dAdap or HW} = \alpha_1 g_i + \alpha_2 c_i + \alpha_3 g_i c_i + \beta \tag{4}$$

where g_i is the $\log_2(CPM + 1)$ of a T-type, c_i is a categorical variable that indicates the class for the ith T-type. The significance of the class-driven effect is indicated by the adjusted p-value for α_3, calculated by the ANOVA test. Considering this class-driven effect, we further reported p-values and slopes for pyramidal cells and interneurons separately by fitting a linear model to only the pyramidal cell data and only the interneuron data, respectively. The details of the analysis are listed in the supplementary table 6 file.

3.6 Differential expression analysis

Differential expression analysis was performed with R 4.2.3 and the DESeq2 package in R (1.36.0) [34]. In analyzing Patch-seq mouse data, genes with q-value < 0.05 and $\log_2(\text{foldchange}) > 1$ are considered differentially expressed genes (DEG). In analyzing UMI macaque monkey data, genes with q-value < 0.01 and $\log_2(\text{foldchange}) > 0.4$ are considered differentially expressed genes (DEG). In estimating the size factor of the macaque monkey, We used the "poscount" option offered by the DESeq2 package

to process the data with lots of zero readouts. Otherwise, we use the default parameters offered by the DESeq2 package.

3.7 Gene Ontology Enrichment

For selected genes, Gene Ontology [3, 2] enrichment analysis is performed using R package clusterProfiler (4.4.4) with the over-representation analysis (ORA) approach[61, 63].

3.8 Hodgkin-Huxley model with Calcium dynamics

We build a Hodgkin-Huxley neuron model with Ca^{2+} dynamics and Ca^{2+} activated K^+ ion channels to reproduce the observed heterogeneity spike-width and degree of adaptation in interneurons. The equations are the following:

$$
\begin{aligned}
C_m \frac{dV}{dt} &= I_{Na} + I_K + I_L + I_{Ca} + I_{AHP} + I_{inj} \\
\frac{d[Ca^{2+}]}{dt} &= -\alpha_{Ca} I_{Ca} - \frac{[Ca^{2+}]}{\tau_{Ca}} \\
I_{Na} &= -g_{Na} m_\infty^3 h (V - V_{Na}) \\
I_K &= -g_K n^4 (V - V_K) \\
I_{Ca} &= -g_{Ca} m_{Ca} (V - V_{Ca}) \\
I_{AHP} &= -g_{AHP} \left(\frac{[Ca^{2+}]}{[Ca^{2+}] + K_d}\right)(V - V_K) \\
I_L &= g_L (V - V_L)
\end{aligned}
$$

Within the equations, g_{Na},g_K,g_{Ca}, g_{AHP} and g_L are corresponding conductance; V_{Na},V_K,V_{Ca}, and V_L are corresponding reversal potentials.

The I_{Na} and I_K are adopted from [55]. The gating variables m, h and n satisfy the first-order kinetics given by:

$$
\frac{dx}{dt} = \phi_x[\alpha_x(V)(1-x) - \beta_x(V)x] = \frac{\phi_x[x_\infty(V) - x]}{\tau_x(V)}
$$

Here, ϕ_x is a temperature factor. For I_{Na}, $m_\infty = \frac{\alpha_m}{\alpha_m + \beta_m}$ where $\alpha_m = \frac{-0.1(V+33)}{\exp(-0.1(V+33))-1}$, $\beta_m = 4\exp(\frac{-(V+58)}{12})$. $\alpha_h = 0.07\exp(\frac{-(V+50)}{10})$ and $\beta_h = \frac{1}{\exp(-0.1(V+20))+1}$. For I_K, $\alpha_n = \frac{-0.01(V+34)}{\exp(-0.1(V+34))-1}$ and $\beta_n = 0.125\exp(\frac{-(V+44)}{25})$.

We adopt the Ca^{2+} dynamics and adaptation current I_{AHP} through the Ca^{2+} activated SK channel from [53], where $m_\infty(V) = \frac{1}{1+\frac{\exp(-(V+20))}{9}}$

We use the following parameter values unless otherwise specified: $C_m = 1\mu\text{F/cm}^2$, $g_L = 0.1\text{mS/cm}^2$, $g_{Na} = 35\text{mS/cm}^2$, $g_K = 9\text{mS/cm}^2$, $g_{Ca} = 1\text{mS/cm}^2$, $g_{AHP} = 5\text{mS/cm}^2$, $V_L = -75\text{mV}$, $V_{Na} = 55\text{mV}$, $V_K = -90\text{mV}$, $V_{Ca} = 120\text{mV}$, $K_d = 30\text{mM}$, $\tau_{Ca} = 80\text{ms}$, $\alpha_{Ca} = 0.001\mu\text{M/ms}\mu\text{A}$.

Simulations designed to reproduce the observed heterogeneity of spike-width and degree of adaptation are done by drawing the conductance of ion channels, $[g_{Na}, g_K, g_{Ca}]$ from a multivariate normal distribution $\mathcal{N}(\mu, \Sigma)$. The mean vector for the distribution is $\mu = [40, 12, 1]$, and the covariance matrix, Σ is computed from a vector of variances $\sigma^2 = [30, 15, 0.15]$ and a correlation matrix given by

$$
R = \begin{pmatrix} 1 & 0.25 & -0.15 \\ 0.25 & 1 & -0.15 \\ -0.15 & -0.15 & 1 \end{pmatrix}
$$

This relationship is formalized as: $\Sigma = \text{diag}(\sigma)(R)\text{diag}(\sigma)$

Acknowledgement

We thank Zhenghan Liao, Panagiota Theodoni, Loïc Magrou, and other members of Xiao-Jing Wang lab for the discussion. We thank Shlomo Dellal, Robert Machold, Chiung-Yin Chung, and other members of Bernardo Rudy lab for the discussion. We thank Shreejoy Tripath for his suggestions and feedback on this work. We thank Julia Sunstrum, Sam Mester, Meghan Wiederman, Sara Matovic, Michelle Jimenez, and Michael Poulter for the electrophysiological data collection of the macaque monkeys. We thank Maximiliano José Nigro for sharing mouse S1 L23 data. We thank Yidi Sun and Juan Meng from ION, Shanghai, for sharing the transcriptomic data of the macaque monkey and for their help with the technique. This work is supported by NIH grant R01MH062349, ONR grant N00014-23-1-2040 and the James Simons Foundation grant NC-GB-CULM-00003138 (to XJW), NIH grants P01NS074972 and R01NS133751 (to BR), CIHR, NSERC, Autism Research Chair province of Ontario NEURONEX (to JMT), the Canadian Institute for Health Research (NGN 171424) in relationship to Neuronex NSF 2015276 and BrainsCAN accelerator grant funded by a Canada First Research Excellence Fund (to WI).

References

[1] Adelman, John P, Maylie, James, and Sah, Pankaj. "Small-conductance Ca2+-activated K+ channels: form and function". In: *Annual review of physiology* 74 (2012), pp. 245–269.

[2] Aleksander, Suzi A et al. "The gene ontology knowledgebase in 2023". In: *Genetics* 224.1 (2023), iyad031.

[3] Ashburner, Michael et al. "Gene ontology: tool for the unification of biology". In: *Nature genetics* 25.1 (2000), pp. 25–29.

[4] Benjamini, Yoav and Hochberg, Yosef. "Controlling the false discovery rate: a practical and powerful approach to multiple testing". In: *Journal of the Royal statistical society: series B (Methodological)* 57.1 (1995), pp. 289–300.

[5] Bock, Tobias and Stuart, Greg J. "The impact of BK channels on cellular excitability depends on their subcellular location". In: *Frontiers in cellular neuroscience* 10 (2016), p. 206.

[6] Bomkamp, Claire et al. "Transcriptomic correlates of electrophysiological and morphological diversity within and across excitatory and inhibitory neuron classes". In: *PLoS computational biology* 15.6 (2019), e1007113.

[7] Capes, EMichelle, Loaiza, Randall, and Valdivia, Héctor H. "Ryanodine receptors". In: *Skeletal muscle* 1 (2011), pp. 1–13.

[8] Carandini, Matteo, Movshon, J Anthony, and Ferster, David. "Pattern adaptation and cross-orientation interactions in the primary visual cortex". In: *Neuropharmacology* 37.4-5 (1998), pp. 501–511.

[9] Catterall, William A et al. "International Union of Pharmacology. XLVIII. Nomenclature and structure-function relationships of voltage-gated calcium channels". In: *Pharmacological reviews* 57.4 (2005), pp. 411–425.

[10] Chambers, J.M. and Hastie, T. *Statistical Models in S*. Wadsworth & Brooks/Cole computer science series. Wadsworth & Brooks/Cole Advanced Books & Software, 1992. ISBN: 9780534167653. URL: https://books.google.com/books?id=uyfvAAAAMAAJ.

[11] Chaudhuri, Rishidev et al. "A large-scale circuit mechanism for hierarchical dynamical processing in the primate cortex". In: *Neuron* 88.2 (2015), pp. 419–431.

[12] Chen, Ao et al. "Single-cell spatial transcriptome reveals cell-type organization in the macaque cortex". In: *Cell* 186.17 (2023), pp. 3726–3743.

[13] Chu, Tianhao et al. "Firing rate adaptation affords place cell theta sweeps, phase precession and procession". In: *eLife* 12 (2024).

[14] Coetzee, William A and Rudy, Bernardo. "Potassium Channels". In: *e LS* (2001).

[15] Cueni, Lucius et al. "T-type Ca2+ channels, SK2 channels and SERCAs gate sleep-related oscillations in thalamic dendrites". In: *Nature neuroscience* 11.6 (2008), pp. 683–692.

[16] Erisir, Alev et al. "Function of specific K+ channels in sustained high-frequency firing of fast-spiking neocortical interneurons". In: *Journal of neurophysiology* 82.5 (1999), pp. 2476–2489.

[17] Fitz, Hartmut et al. "Neuronal spike-rate adaptation supports working memory in language processing". In: *Proceedings of the National Academy of Sciences* 117.34 (2020), pp. 20881–20889.

[18] Froudist-Walsh, Sean et al. "A dopamine gradient controls access to distributed working memory in the large-scale monkey cortex". In: *Neuron* 109.21 (2021), pp. 3500–3520.

[19] Goaillard, Jean-Marc and Marder, Eve. "Ion channel degeneracy, variability, and covariation in neuron and circuit resilience". In: *Annual review of neuroscience* 44 (2021), pp. 335–357.

[20] Gouwens, Nathan W et al. "Integrated morphoelectric and transcriptomic classification of cortical GABAergic cells". In: *Cell* 183.4 (2020), pp. 935–953.

[21] Gu, Ning et al. "Kv7/KCNQ/M and HCN/h, but not KCa2/SK channels, contribute to the somatic medium after-hyperpolarization and excitability control in CA1 hippocampal pyramidal cells". In: *The Journal of physiology* 566.3 (2005), pp. 689–715.

[22] Gu, Yuanzheng et al. "Balanced activity between Kv3 and Nav channels determines fast-spiking in mammalian central neurons". In: *IScience* 9 (2018), pp. 120–137.

[23] He, Miao et al. "Strategies and tools for combinatorial targeting of GABAergic neurons in mouse cerebral cortex". In: *Neuron* 91.6 (2016), pp. 1228–1243.

[24] Huguet, Gemma, Rinzel, John, and Hupé, Jean-Michel. "Noise and adaptation in multistable perception: Noise drives when to switch, adaptation determines percept choice". In: *Journal of vision* 14.3 (2014), pp. 19–19.

[25] Jimenez-Sosa, Michelle Stephanie. *Fast spiking GABAergic interneurons in the dorsolateral prefrontal cortex of non-human primate: Comparison study to mice and human, with focus on subthreshold intrinsic properties*. MSc thesis. https://ir.lib.uwo.ca/etd/7228. 2020.

[26] Jones, Scott L and Stuart, Greg J. "Different calcium sources control somatic versus dendritic SK channel activation during action potentials". In: *Journal of Neuroscience* 33.50 (2013), pp. 19396–19405.

[27] Krienen, Fenna M et al. "A marmoset brain cell census reveals regional specialization of cellular identities". In: *Science Advances* 9 (2023), eadk3986.

[28] Kuznetsova, Marina S, Higgs, Matthew H, and Spain, William J. "Adaptation of firing rate and spike-timing precision in the avian cochlear nucleus". In: *Journal of Neuroscience* 28.46 (2008), pp. 11906–11915.

[29] Lau, David et al. "Impaired fast-spiking, suppressed cortical inhibition, and increased susceptibility to seizures in mice lacking Kv3. 2 K+ channel proteins". In: *Journal of Neuroscience* 20.24 (2000), pp. 9071–9085.

[30] Lee, Brian R et al. "Scaled, high fidelity electrophysiological, morphological, and transcriptomic cell characterization". In: *Elife* 10 (2021), e65482.

[31] Lee, Brian R et al. "Signature morphoelectric properties of diverse GABAergic interneurons in the human neocortex". In: *Science* 382.6667 (2023), eadf6484.

[32] Li, Jennifer Y et al. "Distinct recruitment of feedforward and recurrent pathways across higher-order areas of mouse visual cortex". In: *Current Biology* 31.22 (2021), pp. 5024–5036.

[33] Lipovsek, Marcela et al. "Patch-seq: Past, present, and future". In: *Journal of Neuroscience* 41.5 (2021), pp. 937–946.

[34] Love, Michael I, Huber, Wolfgang, and Anders, Simon. "Moderated estimation of fold change and dispersion for RNA-seq data with DESeq2". In: *Genome biology* 15 (2014), pp. 1–21.

[35] Ma, Xinyue et al. "Modulation of SK channels via calcium buffering tunes intrinsic excitability of parvalbumin interneurons in neuropathic pain: A computational and experimental investigation". In: *Journal of Neuroscience* 43.31 (2023), pp. 5608–5622.

[36] Machold, Robert et al. “Id2 GABAergic interneurons comprise a neglected fourth major group of cortical inhibitory cells”. In: *elife* 12 (2023), e85893.
[37] McCormick, David A et al. “Comparative electrophysiology of pyramidal and sparsely spiny stellate neurons of the neocortex”. In: *Journal of neurophysiology* 54.4 (1985), pp. 782–806.
[38] Meng, John Hongyu et al. “Mechanisms of dominant electrophysiological features of four subtypes of layer 1 interneurons”. In: *Journal of Neuroscience* 43.18 (2023), pp. 3202–3218.
[39] Nigro, Maximiliano José, Hashikawa-Yamasaki, Yoshiko, and Rudy, Bernardo. “Diversity and connectivity of layer 5 somatostatin-expressing interneurons in the mouse barrel cortex”. In: *Journal of Neuroscience* 38.7 (2018), pp. 1622–1633.
[40] Povysheva, Nadezhda V et al. “Electrophysiological heterogeneity of fast-spiking interneurons: chandelier versus basket cells”. In: *PloS one* 8.8 (2013), e70553.
[41] Ripley, Brian D. *Modern applied statistics with S*. springer, 2002.
[42] Rudy, Bernardo and McBain, Chris J. “Kv3 channels: voltage-gated K+ channels designed for high-frequency repetitive firing”. In: *Trends in neurosciences* 24.9 (2001), pp. 517–526.
[43] Salaj, Darjan et al. “Spike frequency adaptation supports network computations on temporally dispersed information”. In: *Elife* 10 (2021), e65459.
[44] Scala, Federico et al. “Phenotypic variation of transcriptomic cell types in mouse motor cortex”. In: *Nature* 598.7879 (2021), pp. 144–150.
[45] Schulz, David J, Goaillard, Jean-Marc, and Marder, Eve. “Variable channel expression in identified single and electrically coupled neurons in different animals”. In: *Nature neuroscience* 9.3 (2006), pp. 356–362.
[46] Shpiro, Asya et al. “Balance between noise and adaptation in competition models of perceptual bistability”. In: *Journal of computational neuroscience* 27 (2009), pp. 37–54.
[47] Storm, Johan F. “Action potential repolarization and a fast after-hyperpolarization in rat hippocampal pyramidal cells.” In: *The Journal of physiology* 385.1 (1987), pp. 733–759.
[48] Tasic, Bosiljka et al. “Shared and distinct transcriptomic cell types across neocortical areas”. In: *Nature* 563.7729 (2018), pp. 72–78.
[49] Torres-Gomez, Santiago et al. “Changes in the proportion of inhibitory interneuron types from sensory to executive areas of the primate neocortex: implications for the origins of working memory representations”. In: *Cerebral Cortex* 30.8 (2020), pp. 4544–4562.
[50] Tremblay, Robin, Lee, Soohyun, and Rudy, Bernardo. “GABAergic interneurons in the neocortex: from cellular properties to circuits”. In: *Neuron* 91.2 (2016), pp. 260–292.
[51] Tripathy, Shreejoy J et al. “Assessing transcriptome quality in patch-seq datasets”. In: *Frontiers in Molecular Neuroscience* 11 (2018), p. 363.
[52] Tripathy, Shreejoy J et al. “Transcriptomic correlates of neuron electrophysiological diversity”. In: *PLoS computational biology* 13.10 (2017), e1005814.
[53] Wang, Xiao-Jing. “Calcium coding and adaptive temporal computation in cortical pyramidal neurons”. In: *Journal of Neurophysiology* 79.3 (1998), pp. 1549–1566.
[54] Wang, Xiao-Jing. “Theory of the multiregional neocortex: large-scale neural dynamics and distributed cognition”. In: *Annual review of neuroscience* 45 (2022), pp. 533–560.
[55] Wang, Xiao-Jing and Buzsáki, György. “Gamma oscillation by synaptic inhibition in a hippocampal interneuronal network model”. In: *Journal of neuroscience* 16.20 (1996), pp. 6402–6413.
[56] Weber, Alison I, Krishnamurthy, Kamesh, and Fairhall, Adrienne L. “Coding principles in adaptation”. In: *Annual Review of Vision Science* 5 (2019), pp. 427–449.
[57] Willmore, Ben DB and King, Andrew J. “Adaptation in auditory processing”. In: *Physiological Reviews* 103.2 (2023), pp. 1025–1058.
[58] Wilson, Rachel I and Mainen, Zachary F. “Early events in olfactory processing”. In: *Annu. Rev. Neurosci.* 29 (2006), pp. 163–201.

[59] Wolfart, Jakob and Roeper, Jochen. "Selective coupling of T-type calcium channels to SK potassium channels prevents intrinsic bursting in dopaminergic midbrain neurons". In: *Journal of Neuroscience* 22.9 (2002), pp. 3404–3413.

[60] Wonders, Carl P et al. "A spatial bias for the origins of interneuron subgroups within the medial ganglionic eminence". In: *Developmental biology* 314.1 (2008), pp. 127–136.

[61] Wu, Tianzhi et al. "clusterProfiler 4.0: A universal enrichment tool for interpreting omics data". In: *The innovation* 2.3 (2021).

[62] Yao, Zizhen et al. "A taxonomy of transcriptomic cell types across the isocortex and hippocampal formation". In: *Cell* 184.12 (2021), pp. 3222–3241.

[63] Yu, Guangchuang et al. "clusterProfiler: an R package for comparing biological themes among gene clusters". In: *Omics: a journal of integrative biology* 16.5 (2012), pp. 284–287.

E Feature	θ	$ACCY_1$	θ_l	θ_r	$ACCY_2$	$\%Lost$	N_{PV}	N_{SST}
dAdap	0.349	92.3%	0.293	0.383	95.9%	9.5%	278	1105
HW(ms)	0.360	89.6%	0.327	0.399	92.4%	16.0%	840	1813

Table 1 Extended Data Table 1. Performance of single-parameter classifiers. θ indicates the optimal value for classifying PV and SST cells with performance $ACCY_1$. θ_l and θ_r indicate an optimal way of classification with performance $ACCY_2$ by excluding $\%Lost$ of borderline cells in the total population. The sample sizes are indicated by N_{PV}, N_{SST}. See the method for details.

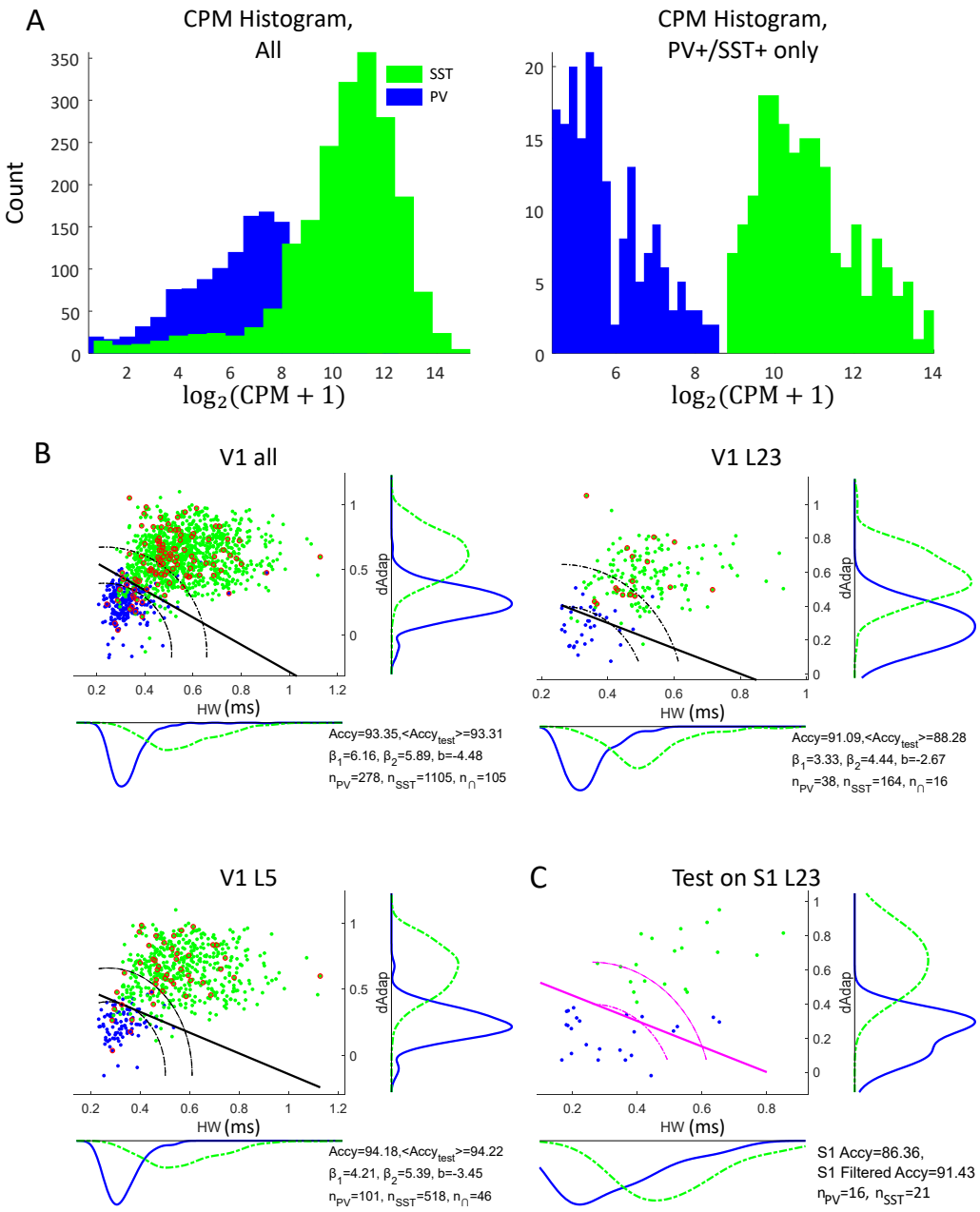

Fig. 9 Extended Data Figure 1. Performance of trained classifier compared to that of the marker gene classification. (A) distribution of the *Pvalb* and *Sst* markers. Left: Histogram of *Pvalb* and *Sst* in all cells. Right: Histogram of cells that are both *Pvalb*+ and *Sst*+. A cell with *PV* larger than the 20 percentile of the total distribution ($\theta_{PV} = 4.49$) counts as *Pvalb*+. The same applies for *Sst*+ ($\theta_{SST} = 8.97$). In the dataset, a total of 1025 *Pvalb*+ cells and 1604 *SST*+ cells are identified. Within those, 189 cells are identified as *Pvalb*+/*Sst*+. The CPM distributions of these 189 cells are shown on the right. If considering multiple-gene classification as the ground truth, then the accuracy of the gene-marker (PV and SST marker) classification is 89.62%. (B) Classification of PV and SST based on HW and dAdap across layers. The solid line represents the classification boundary, indicated by $y = -(x\beta_1 + b)/\beta_2$. The red circle represents *Pvalb*+/*Sst*+ cells. Notice that these cells are not only distributed close to the boundary. Dashed line, the 95% confidence boundary based on the Gaussian mixture model. See supplementary table 1 for details. (C) Test the trained classifier from V1 on a dataset from the somatosensory cortex. The filtered accuracy represents the classifier accuracy after excluding low-confidence cells. I.e., excluding the cells within the two dashed pink lines.

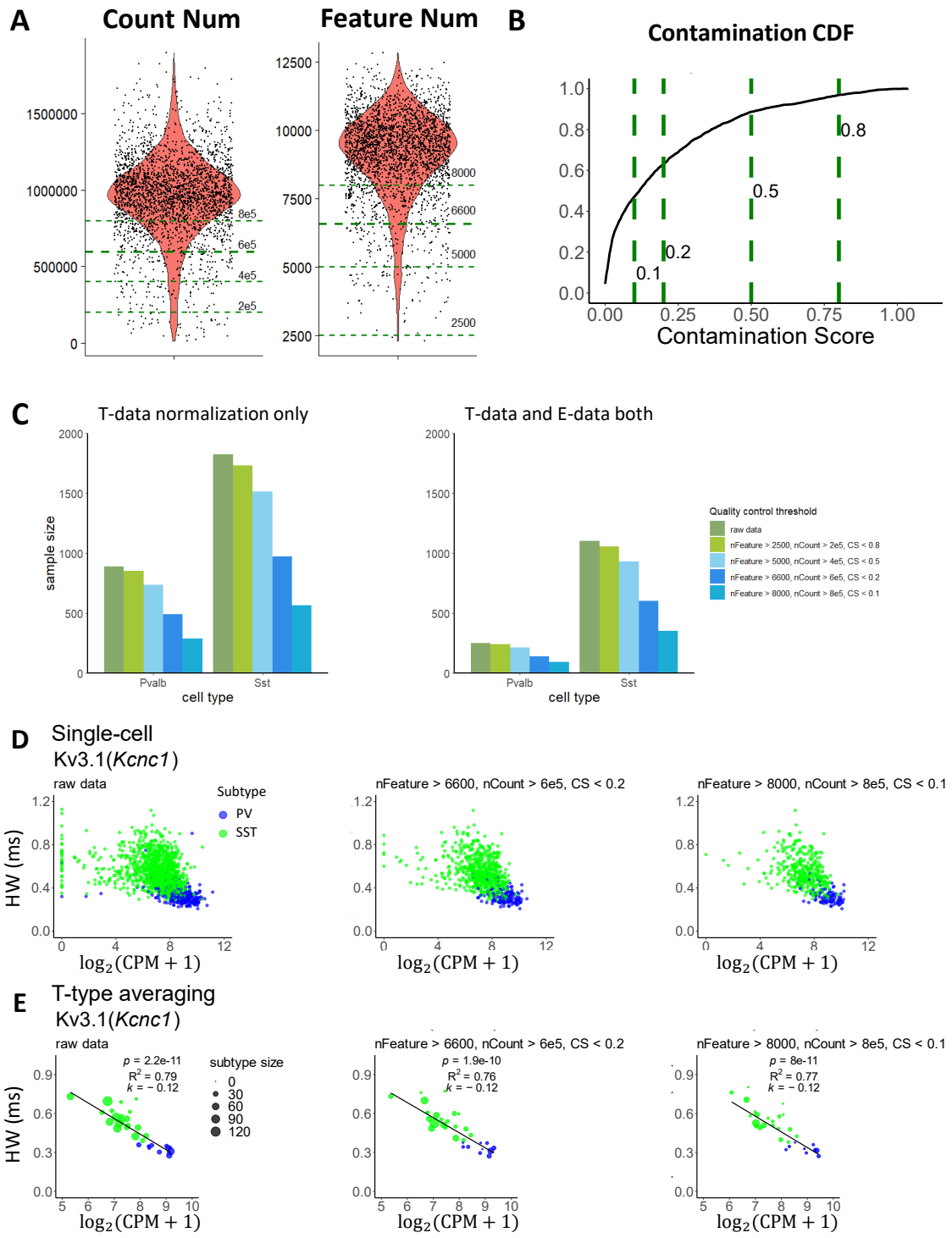

Fig. 10 Extended Data Figure 2. Quality control of transcriptomic data with different thresholds. (A) Violin plot for V1 raw count data: number of total raw counts per cell (nCount_RNA, left) and number of unique sequenced genes per cell (nFeature_RNA, right). Dashed lines represent different thresholds. (B) Cumulative distribution function for the contamination score. (C) Histogram of the number of cells (sample size) that passed the corresponding quality control parameters before (left) and after (right) merging with cells that also passed the electrophysiological quality control. The parameter sets are colored. (D, E) Scatter plot at the single cell level (D) and at the T-type level (E) of the HW and *Kcnc1* with different quality control parameters. Strict quality control reduces dropout issues (zero readouts along the y-axis) at the single-cell level, while T-type level performances are comparable.

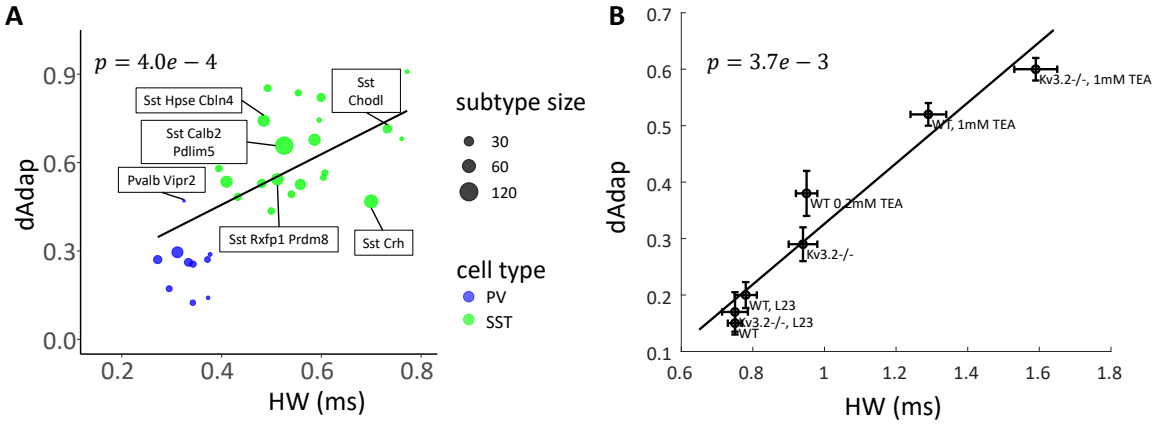

Fig. 11 Extended Data Figure 3. Correlation between HW and dAdap. (A) data from the mouse V1 Patch-seq dataset. Different dots represent different transcriptomic-defined subtypes. The T-type annotation is the same as in [20]. Different T-types show different morphological features. For example, *Pvalb Vipr2* corresponds to chandelier cells, showing a larger dAdap, consistent with [40]. The details can be found in the supplementary table 2. (B) data from a mouse M1 dataset. This figure is generated from data of [29], collected at room temperature from L5/6 unless specified otherwise. The HW and dAdap increase with Kv3.2 gene knockout or with inhibiting the Kv3 family by applying TEA. The standard deviation is indicated by error bars.

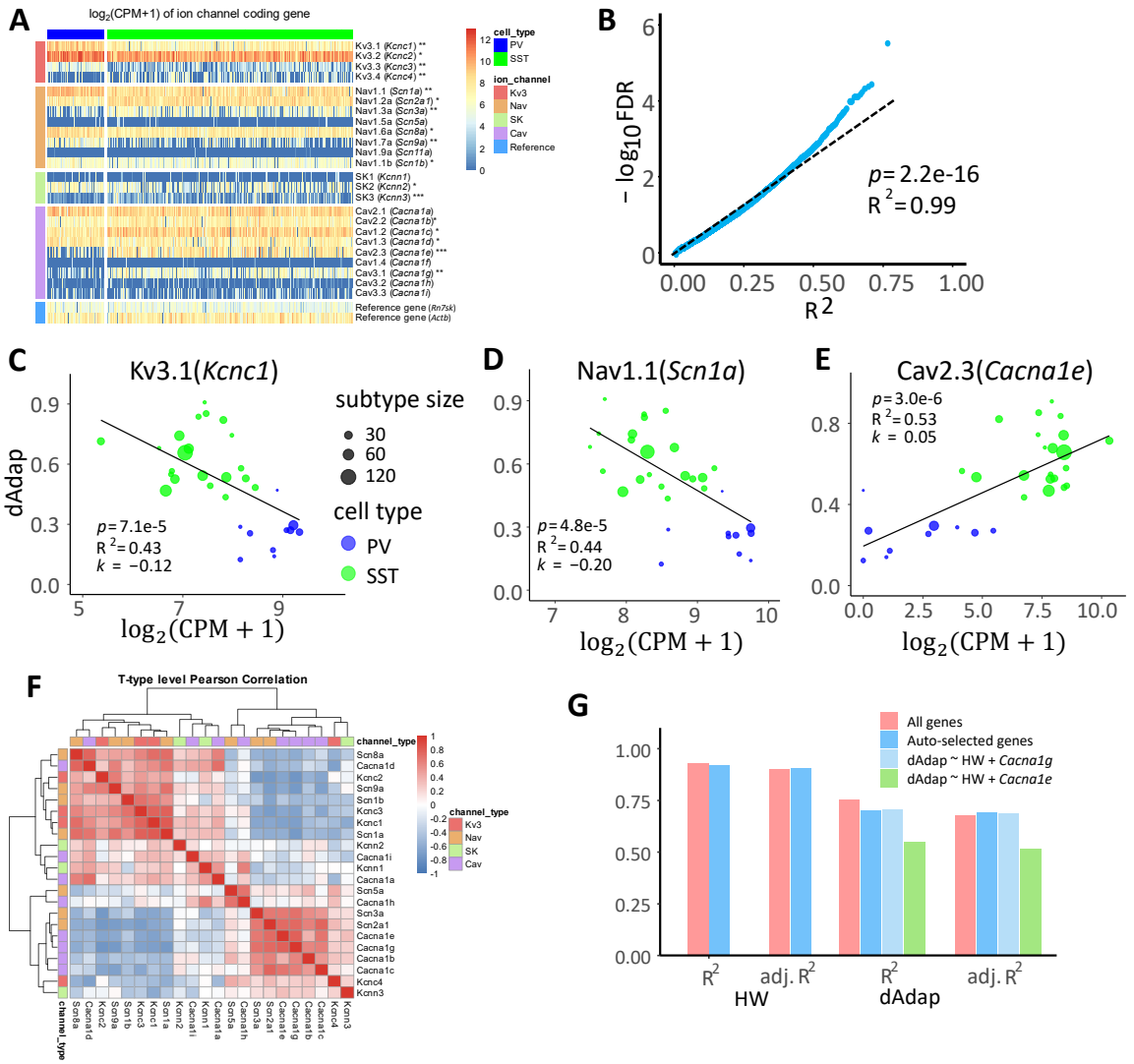

Fig. 12 Extended Data Figure 4. Further analyses of directly related genes. (A) Differential expression analysis. The expression of genes $\log_2(+1)$ is shown in different colors. Asterisks are used to annotate differences in gene expression between V1 PV and SST cells. All annotated genes have a q value smaller than 0.05. The asterisks represent the fold change between cell types (*: fold change between 0.5 and 1, **: 1 to 2, ***: >2). In our analysis, genes with $q < 0.05$ and fold change larger than one were counted as DEGs. (B) R^2 and -lg(FDR) of all genes' WLR results are linearly correlated. FDR: False discovery rate with correction for multi-hypothesis, using the Benjamini-Hochberg method. (C) Correlation between Adap and *Kcnc1* at T-type level. (D) dAdap and *Scn1a*. (E) dAdap and *Cacna1e*. (F) Person correlation of selected ion channel coding genes normalized T-type average expression level. (G) Bar plot for R^2 and adjusted R^2 for different WLR models. See Methods.

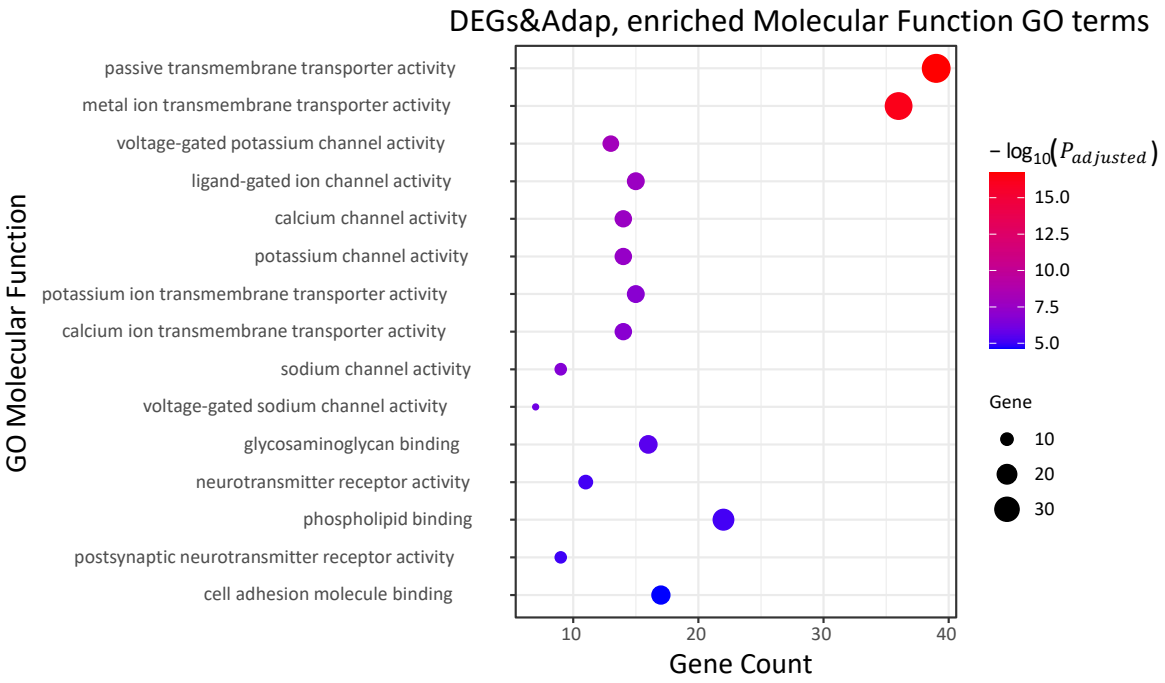

Fig. 13 Extended Data Figure 5. Gene Ontology enrichment analysis. The top 15 terms of molecular function from the genes are DEGs and are highly correlated with dAdap. The X-axis and size of the bubble represent the number of selected genes enriched in the corresponding GO term. Color is used to show the significance of each enriched GO term. The full list is in the supplementary table 5.

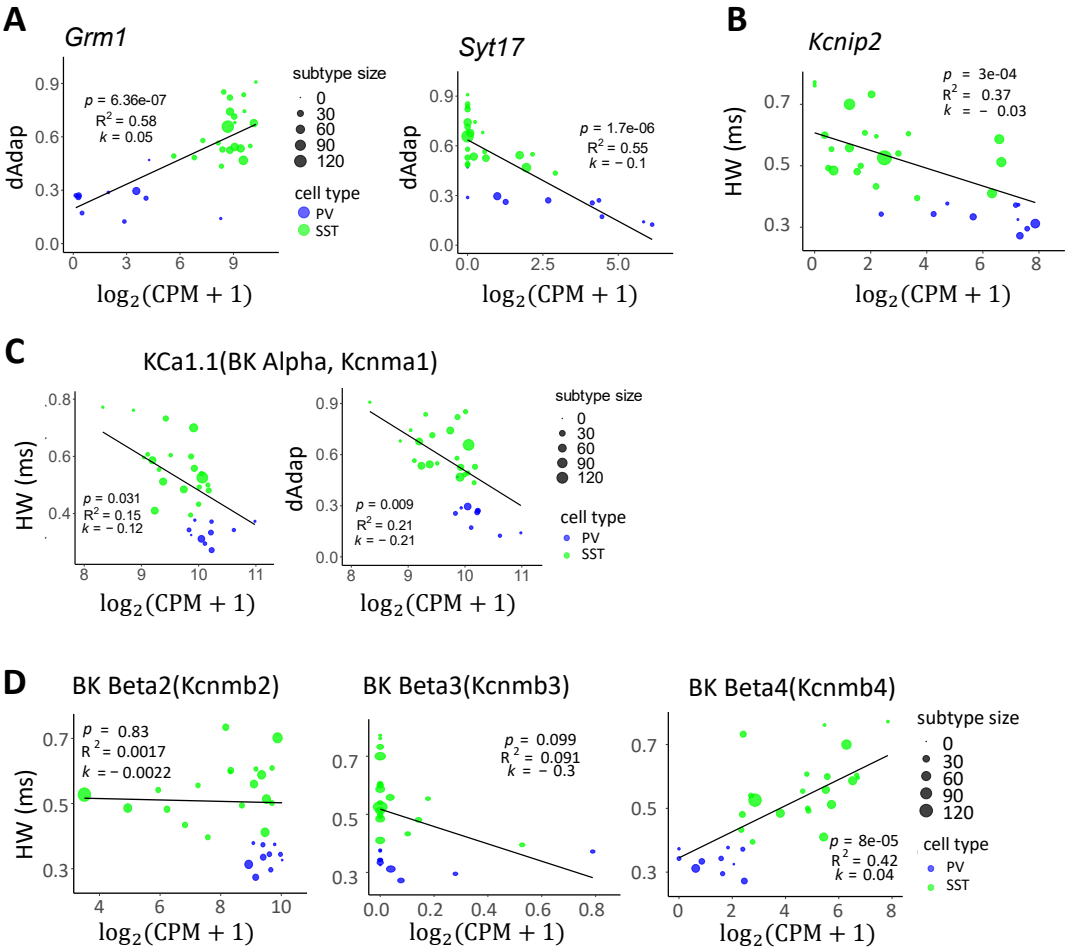

Fig. 14 Extended Data Figure 6. More WLR on example genes. (A) *Grm1* and *Syt17* are highly correlated with dAdap. (B) *Kcnip2* is significantly correlated with HW. (C) *Kcnma1*, encoding alpha-unit of big-conductance K^+ (BK) channel, are weakly correlated with HW and dAdap. (D) *Kcnmb2* to *Kcnmb4*, encoding beta-units of the BK channel, do not consistently correlate with HW

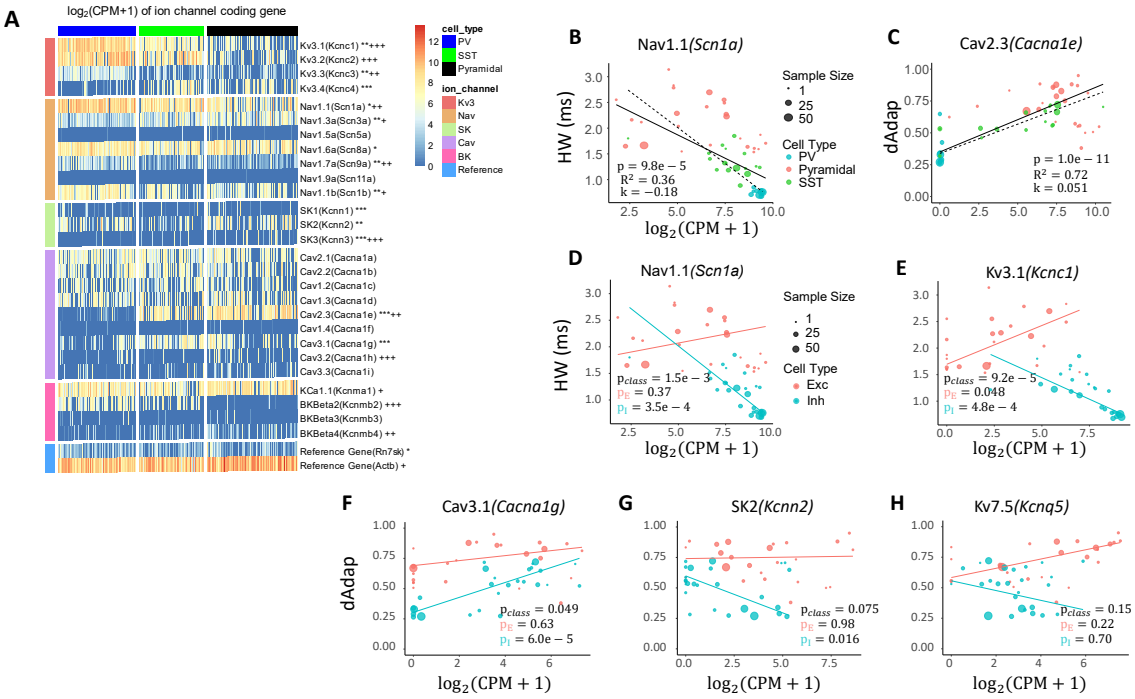

Fig. 15 Extended Data Figure 7. Further analyses on the mouse M1 dataset. (A) Differential expression analysis as in Extended Data Figure 12F. The asterisks and crosses represent the fold change between PV and SST, or INs and pyramidal cells, respectively (*/+: fold change between 0.5 and 1, **/++: 1 to 2, ***/+++: > 2). (B) Correlation between *Scn1a* and HW. (C) *Cacna1e* and dAdap. (D to H) Class-dependent effect of different genes. p_{class} shows the significance of the class-dependent effect; p_E and p_I show the significance of a non-zero slope in the I and E subsets, respectively. (D) Correlation between *Scn1a* and HW. (E) *Kcnc1* and HW. (F) *Cacna1g* and dAdap. (G) *Kcnn2* and dAdap. (H) *Kcnq5* and dAdap

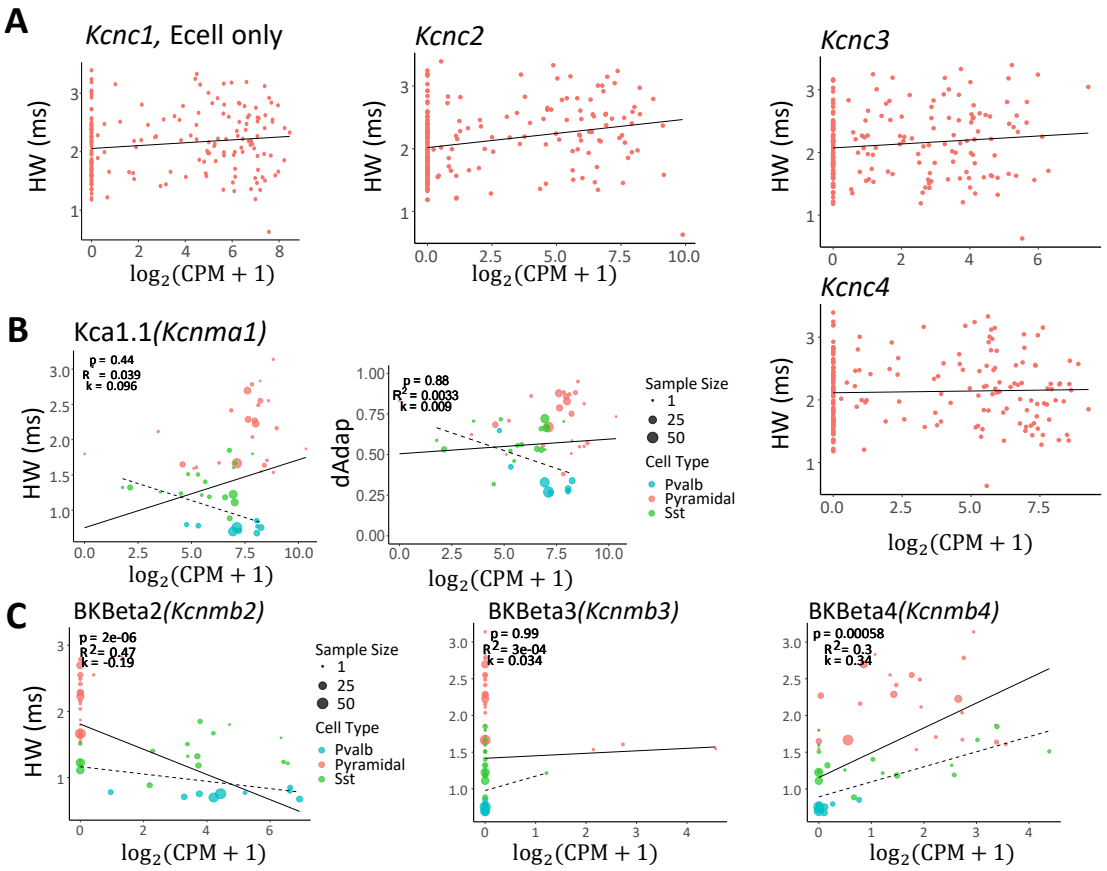

Fig. 16 Extended Data Figure 8. HW differences in M1 pyramidal cells can not be explained by other K channels. (A) correlation between Kv3 encoding genes (*Kcnc1* to *Kcnc4*) and HW at the single cell level for pyramidal cells. All non-zero slopes are non-significant. (B) Correlation between BK alpha unit *Kcnma1* and HW or dAdap. (C) Correlation between BK beta unit *Kcnmb2* to *Kcnmb4* and HW. Based on (B, C), BK encoding genes cannot explain the observed HW difference within pyramidal cells.

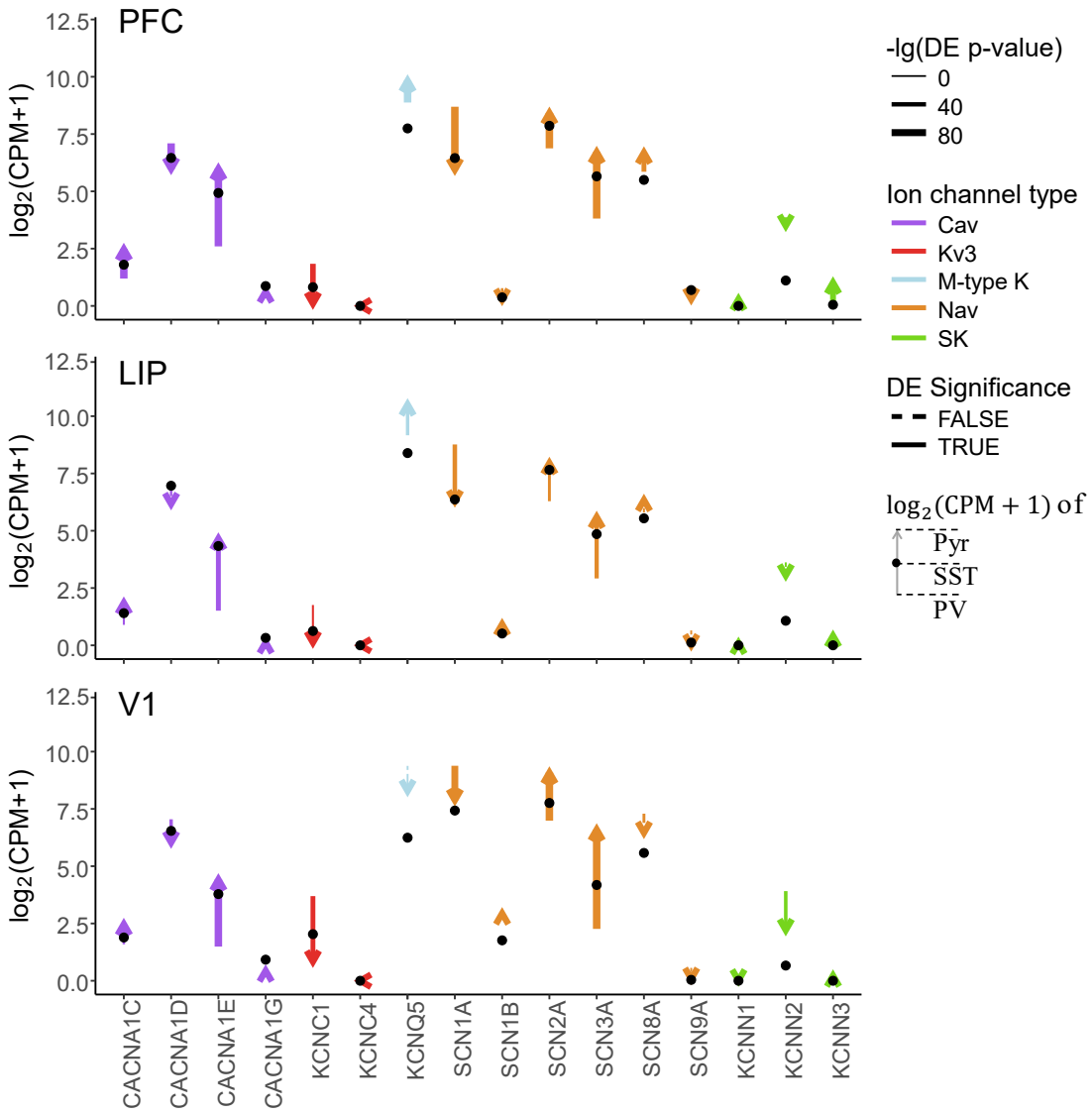

Fig. 17 Extended Data Figure 9. Transcriptomic differences across cell types from the macaque monkey dataset in PFC (top), LIP (middle), and V1 (bottom) across Pyramidal cells, PV and SST INs. Each arrow represents one gene, starting from the trimmed mean of PV INs and pointing to that of pyramidal cells. The black dot on the arrow indicates the trimmed mean of SST INs. The significance is indicated by solid arrows with DE analysis $q < 0.01$ and $|log_2(\text{Fold Change})| \geq 0.4$. More genes are significantly different across cell types than across brain regions (Figure 7C). Noticing the M-type cannot explain IN dAdap differences since the SST expression (black dot) is lower than the PV expression (start of the arrow).